

THERMAL TRANSPORT PROPERTIES OF GRAPHENE WITH
HYDROGENATION DOPING BY MOLECULAR DYNAMICS
SIMULATIONS

A Dissertation
Presented to
the Graduate School of
Clemson University

In Partial Fulfillment
of the Requirements for the Degree
Doctor of Philosophy
Mechanical Engineering

by
Chengjian Li
August 2015

Accepted by:
Dr. Huijuan Zhao, Committee Chair
Dr. Gang Li, Co-chair
Dr. Srikanth Pilla
Dr. Lonny L. Thompson

ProQuest Number: 3722410

All rights reserved

INFORMATION TO ALL USERS

The quality of this reproduction is dependent upon the quality of the copy submitted.

In the unlikely event that the author did not send a complete manuscript and there are missing pages, these will be noted. Also, if material had to be removed, a note will indicate the deletion.



ProQuest 3722410

Published by ProQuest LLC (2015). Copyright of the Dissertation is held by the Author.

All rights reserved.

This work is protected against unauthorized copying under Title 17, United States Code
Microform Edition © ProQuest LLC.

ProQuest LLC.
789 East Eisenhower Parkway
P.O. Box 1346
Ann Arbor, MI 48106 - 1346

ABSTRACT

Thermal transport properties of graphene are of significance and have been widely discussed since first discovery of graphene in the early 2000s. Recently, chemical functionalization of graphene for controllable and reversible tuning of its material properties has drawn tremendous interests. The theoretical and experimental progress on controlled hydrogenation of graphene creates an opportunity for a more precise tuning of its physical properties, including the thermal transport properties. In addition, various doping patterns can also induce geometry change and thermal rectification in graphene. With the ability to control thermal rectification in graphene through chemical functionalization, more novel applications in thermal transistors, thermal logic circuits that are essential for thermal memory and computation can be developed. However, while patterned chemical functionalization is being recognized as an effective way to modify or control the material properties of graphene for various applications, the fundamental physical mechanisms underlying the thermal conductivity variation, geometry change and thermal rectification due to patterned hydrogen doping has not been well understood.

In this work, we focus on the study of thermal transport properties of graphene with various doping configurations including symmetric and asymmetric single-side and double-side patterned hydrogenation, as well as patterned doping using other types of atoms such as boron. Through non-equilibrium molecular dynamics (NEMD) simulation based theoretical and numerical analysis, we calculate thermal transport properties of the chemical functionalized graphene including thermal conductivity, phonon dispersion

relation, phonon density of states, phonon relaxation time and specific heat. By analyzing the relation between these physical quantities and the doping parameters, the physical mechanisms through which the doping configurations alter the thermal transport behavior are revealed.

For single-side doped graphene, we demonstrate that various deformation modes can be induced and these deformation modes can be controlled by the hydrogenation patterning parameters. Both the doping density and morphology contribute to the thermal conductivity variation of the graphene sheet. With the control of hydrogenation patterning parameters, desired deformation modes and thermal conductivity of graphene can be achieved. For double-side doped graphene, we show that the thermal conductivity decreases with increasing hydrogen doping coverage. The decreasing rate, however, depends on the doping orientation. Our results show that, while hydrogenation has little effect on the specific heat, it decreases the phonon group velocity and increases phonon-phonon scattering in graphene. The phonon group velocity reduction is only due to the increment of doping coverage and is independent of doping orientation. Larger angle between the doping stripe orientation and the heat flux direction leads to smaller relaxation times, i.e., stronger phonon-phonon scattering, resulting in a lower thermal conductivity. Finally, we demonstrate that triangular doping pattern causes asymmetry of geometry and mass in graphene, and thus induces thermal rectification in the doped graphene. The fundamental cause of the thermal rectification is being studied by using our NEMD simulation data and the kinetic theory for lattice thermal transport.

ACKNOWLEDGEMENTS

I would like to express my sincere gratitude to all those who have been helpful to me during my PhD program. It is impossible to complete this thesis without their gracious help.

First and foremost, I would like to thank my advisor Dr. Huijuan Zhao and co-advisor Dr. Gang Li for their great support, guidance, patience, encouragement, and insightful advice over the past years. Dr. Zhao has always been insightful, responsive and supportive. Her strong background in solid mechanics, her expertise in molecular dynamics, her ability in identifying problems and finding solutions have been so useful to me that I can build a deep understanding in the field of study. Dr. Li enlightened me the vision of multi-scale modelling, numerical methods and nano-materials, encouraged me with enthusiasm and determination when I encountered difficult problems, closely supervised me when I got stuck, and guided me through the project. I deeply acknowledge my gratitude and profound respect to both of them.

I would also like to extend my true appreciation to my committee members, Dr. Srikanth Pilla and Dr. Lonny L. Thompson. I would like to thank them for serving on my dissertation committee, reading my thesis and commenting on my work. Also I really enjoyed the FEA course Dr. Thompson taught and I am very thankful to him for the discussion about course project.

Furthermore, I would like to thank my colleagues, Hua Li, Jun Lan, Qi Liu, Ying Yu, Jixuan Gong, Yingye Gan, Shanyun Gao and Qian Mao for numerous helpful

discussion in my work and assistance in my life. I would like to thank my friends around Clemson for making my life here more interesting.

My special acknowledgement goes to my family. I would like thank my parents and sister for all their understanding, support, encouragement and love.

TABLE OF CONTENTS

	Page
TITLE PAGE	i
ABSTRACT	ii
ACKNOWLEDGEMENTS	iv
LIST OF TABLES	viii
LIST OF FIGURES	ix
Chapter 1 INTRODUCTION	1
Chapter 2 METHOD	6
2.1 Molecular Dynamics	8
2.3 Thermal Conductivity	13
2.4 Phonon Density of States	15
2.5 Specific Heat	15
2.6 Spectral Energy Density	16
2.7 Phonon Relaxation Time	18
Chapter 3 THERMAL TRANSPORT PROPERTIES OF PRISTINE GRAPHENE.....	20
3.1 Size Effect on Thermal Conductivity of Pristine Graphene.....	20
3.2 Strain Effect on Thermal Conductivity of Pristine Graphene	22
3.3 Temperature Effect on Thermal Conductivity of Pristine Graphene	25
Chapter 4 HYDROGENATION INDUCED DEFORMATION MODE AND THERMAL CONDUCTIVITY VARIATIONS IN GRAPHENE SHEETS	28
4.1 Simulation details	28
4.2 Deformation Mode Induced By Single-Side Hydrogenation	32
4.3 Thermal Conductivity Variation with Double-Side Hydrogenation Stripes	36

Table of Contents (Continued)

	Page
4.4 Thermal Conductivity Variation with Double-Side Hydrogenation Blocks	38
4.5 Thermal Conductivity Variation with Single-Side Hydrogenation Patterns....	40
4.6 Summary	43
Chapter 5 THERMAL CONDUCTIVITY VARIATION OF	
GRAPHENE WITH PATTERNED DOUBLE-SIDE	
HYDROGENATION.....	45
5.1 Simulation Setup	45
5.2 Thermal Conductivity	47
5.3 Phonon Dispersion	50
5.4 Phonon Relaxation Time.....	54
5.5 Phonon Density of States and Specific Heat.....	57
5.6 Summary	60
Chapter 6 THERMAL RECTIFICATION IN GRAPHENE WITH	
TRIANGLE DOPING PATTERN.....	61
6.1 Molecular Dynamics Setup	62
6.2 Thermal Rectification of Triangular Hydrogenated Graphene under Strain	
Effect.....	63
6.3 Thermal Rectification Controlling Parameters	65
6.4 Summary	77
Chapter 7 CONCLUSIONS.....	78
REFERENCES	81

LIST OF TABLES

Table 1 Elastic properties of Carbon, Silicon bonds in Tersoff potential, with unit in Mbar	
.....	73

LIST OF FIGURES

Figure 1: Phonon thermal transport models.....	6
Figure 2: Schematic diagram of a graphene sheet for the calculation of thermal conductivity. The graphene sheet has one cold region (blue), two heat flux regions (green) and one hot region (red).	13
Figure 3: Size effect of thermal conductivity. (a) TC variation as a function of width (length = 19.8 and 19.6 nm for armchair and zigzag graphene, respectively), (b) TC variation as a function of length (width = 4.9 and 5nm for armchair and zigzag graphene, respectively).	21
Figure 4: Thermal conductivity of graphene with tensile and compressive strain.	23
Figure 5: Phonon density of states for graphene under tension and compression.	24
Figure 6: Variation of thermal conductivity of graphene as a function of temperatures..	25
Figure 7: Normalized PDOS of graphene at different temperatures, size = 5 nm × 39.2 nm.	26
Figure 8: (color online) (A) schematic diagram of patterned double-side hydrogenation; (B) schematic diagram of patterned single-side hydrogenation; (C-F) deformation modes induced by patterned single-side hydrogenation: (C) TRI mode, (D) COM mode, (E) aROL mode and (F) ROL mode.	31
Figure 9: (color online) (A) slope q variation with hydrogenation length W; (B-G) schematic diagrams of the beam bending model (E, F, G) with the corresponding force and moment calculated from the first principles theory (B, C, D).	33
Figure 10: (A) Thermal conductivity variation as a function of doping coverage with longitudinal and transverse hydrogenation patterns; (B) PDOS under various doping coverage conditions with longitudinal and transverse hydrogenation patterns; (C) Acoustic phonon velocity variation as a function of the transverse doping coverage.	36
Figure 11: Schematic diagram of doping blocks on graphene.....	38
Figure 12: Graphene TC varies with coverage and number of blocks.	39

- Figure 13: Thermal conductivity variation with hydrogenation length W and stripe length H . The graphene sheet has the size of $5.10 \text{ nm} \times 19.65 \text{ nm}$. The size of empty circles represents the magnitude of thermal conductivity of the unrelaxed graphene sheet with patterned hydrogenation. The size and color of the filled circles represent the magnitude of thermal conductivity and the deformation mode of the relaxed graphene sheet with patterned hydrogenation..... 42
- Figure 14: Comparison of PDOS between unrelaxed (solid line) and relaxed (dash line) graphene with various hydrogenation length W . The length of the stripe H is 4.91 nm 43
- Figure 15: Schematic NEMD model of graphene with the heat source region (red, δ is the width of the region), heat sink regions (blue), and heat flux regions (cyan). (a) pristine graphene; (b) longitudinal hydrogen doping stripes (0 degree); (c) 30 degree angular hydrogen doping stripes; and (d) transverse hydrogen doping stripes (90 degree). The subplot in (d) represents the graphene lattice with hydrogen doping (C: cyan, H: yellow). All the black dash boxes represent the unit cell for SED calculation, respectively..... 48
- Figure 16: Thermal conductivity of graphene with longitudinal (0 degree), transverse (90 degree) and 30 degree angular doping stripes..... 49
- Figure 17: Dispersion relation of zigzag graphene with doping stripe angle of 0 degree (top) and 90 degree (bottom), $aS = 3aC - C$ and $aL = 403aC - C$ are lattice constants of small and large unit cell..... 53
- Figure 18: (a) Dispersion relation of pristine graphene; (b) spectral energy density of pristine graphene with $k^* = 0, 0.5$, and 1 ($k^* = kas/\pi$), $as = 3aC - C$. Blue dots are the phonon SED, red lines are fitted to SED peaks to extract phonon relaxation time τ 54
- Figure 19: Frequency dependent relaxation time of graphene with hydrogen doping stripes, with doping coverage ranging from 0% to 100%. (b)-(d) also show relaxation time comparisons between 0 and 90 degree doping stripe orientations. (f) represents the comparison between 0% doping and 100% doping case. 56

Figure 20: Phonon density of states variation with selective doping coverage and orientation	58
Figure 21: Temperature dependence of specific heat of pristine and longitudinally doped graphene.	59
Figure 22: Schematic model of graphene with triangle doping pattern.	62
Figure 23 Thermal conductivity (a) and thermal rectification (b) of triangular doped graphene in Fig. 22.	63
Figure 24 Total PDOS of triangular doped graphene with $J +$ and $J -$	64
Figure 25 Thermal conductivity (b) and thermal rectification (c) of 30 degree triangular doped graphene (a).	66
Figure 26 Thermal conductivity (a) of 60 degree triangular doped graphene with and comparison of thermal rectification (b) of triangular doped graphene with 5×19.6 nm (L1) and that with 10×39.3 nm (L2).	67
Figure 27 Mass effect on temperature profile with different heat flux direction. (a): $J +$ heat flux direction is from the center to the edge; (b) $J -$ heat flux direction is from the edge to the center. Legend shows atomic mass ratio changes from 0.08 to 8.	69
Figure 28 Thermal conductivity (a) and thermal rectification (b) of triangle patterned graphene of various masses.	70
Figure 29 Local PDOS of graphene with various mass ratios in two opposite heat flux directions. Atomic mass ration changes from 0.08 to 8.	71
Figure 30 Silicene model with buckled honeycomb lattice structure where Si-Si bond length is 2.28 \AA [125], and the buckling parameter δ is 0.45 \AA [126]	72
Figure 31 Thermal conductivity (a) of silicene and comparison thermal rectification (b) of silicene and graphene model with triangle doping pattern of various atomic mass	74
Figure 32 Silicon-Carbon model, carbon atoms are magnate dots in the triangle pattern, silicon atoms the matrix are bonded but not shown in the figure. The red bar and blue bar represent the hot region and cold region, and vice versa.	76

CHAPTER 1 INTRODUCTION

In recent years, due to the advance of manufacturing technology, nanomaterials have been extensively used in ultra-small devices [1], [2] [cite some review papers]. Broadly defined, nanomaterials are those which have constituents or structured components with at least one dimension in size range from approximately 1 to 100 nm. Excellent mechanical, electronic, thermal and optical properties in nanomaterials have been reported [3]–[9], which are expected to advance the development of technologies in many areas, ranging from semiconductor, automotive, aerospace industries to medical and research labs. The thermal transport properties of nanomaterials are of particular importance in the performance of nanomaterial based devices and systems. For example, it is critical to control the heat dissipation in microelectronic devices due to the arising thermal management problems in miniaturization. Furthermore, thermal operations, such as thermal rectification, thermal transistor and thermal logic gate, will extend the applications of nanomaterials to an even more promising field. Future prosperity of many industries such as information technology, energy, medical and manufacturing, relies heavily on how well the nanomaterials are understood and integrated into large systems.

As a two-dimensional nanomaterial having a honeycomb lattice structure, graphene has exhibited supreme mechanical,[3][4][10][11] electronic,[5][6] optical[7] and thermal[8][9] properties to ensure it as one of the most promising materials in next-generation of nano and micro devices and applications[12]–[15]. The structural flexibility and superior material properties of graphene make it a desirable material in the

development of next generation integrated circuits, electronics and ultra-small sensors[12]. Since miniaturization drives future electronic devices, heat dissipation and energy conversion efficiency are critical in two dimensional electronic circuit applications. Graphene based transparent flexible heater shows better time-dependent temperature profile than other material based heaters.[16] New applications in vehicle front-window defrosters are possible thanks to the excellent temperature versus power density performance in graphene-based heating system.[17] Other applications where thermal transport in graphene plays an important role include graphene-based thermal interface materials [18], transparent graphene electrodes in photovoltaic solar cells [13], and graphene-based nanosensors [19], just to name a few.

Thermal transport properties of graphene are of significance and have been widely discussed since first discovery of graphene in the early 2000s [20]. Experimental results indicate that suspended single-layer graphene at room temperature exhibits extremely high thermal conductivity (TC), up to 5300 W/m-K [8]. The excellent heat conduction ability of graphene will improve performance of self-heat densely packed devices[21]. However, TC of graphene is subjective to many factors, including strain[22], temperature[23], defects[24], functionalization[25], *etc.* Recently, chemical functionalization of graphene for controllable and reversible tuning of its material properties has drawn tremendous interests [26]–[29]. Among various types of chemical functionalization, hydrogenation of graphene has been investigated extensively due to its relevance to hydrogen storage as well as its scientific and practical importance for chemistry [28]. Theoretical and experimental studies have shown that electronic and magnetic properties of graphene can be modified

by using various hydrogenation approaches[29]–[33]. Since then, significant progress has been made experimentally on controlled hydrogenation of graphene, such as single-sided hydrogenation of pristine graphene [34] and controlled hydrogenation patterning of graphene [35]. The theoretical and experimental progress on controlled hydrogenation of graphene creates an opportunity for a more precise tuning of its physical properties, including the thermal transport properties. It has been demonstrated that TC of graphene significantly decreases with doping hydrogen atoms due to localized change in atomic bonds.[36][37] Various doping patterns can also induce geometry change[38] and thermal rectification[39] in graphene. While patterned hydrogenation is being recognized as an effective way to modify or control the material properties of graphene for various applications, the fundamental physical mechanisms of graphene TC variation due to patterned hydrogen doping has not been well understood.

Thermal rectification is a phenomenon that thermal conductivity of material in certain direction differs with that in the reverse direction. It can be dated back to 1936 when Starr [40] disclosed this asymmetrical thermal conductance in his experiment. There have been many researches ever since Starr's discovery. It sees an explosion of theoretical studies,[41]–[53] especially molecular dynamics simulations, on this topic after Chang[54] demonstrated in his experiment, the solid-state thermal rectification in carbon nanotube with non-uniform axial mass distribution. In area of thermal management, which is an important section of graphene application, graphene can help improving heat dissipation in density packed devices. Thermal rectification (TR) in graphene can be observed as soon as nonlinear interaction and asymmetry are available[44]. Rajabpour[39] reports that TR

in graphene-graphane nanoribbons is about 25%. Yang[52] finds that overlap of power spectra of two separate layers cause thermal rectification in nitrogen-doped graphene. With the ability to control thermal rectification in graphene, more novel applications in thermal transistors, thermal logic circuits that are essential for thermal memory and computation can be developed. Unfortunately, the fundamental physical mechanisms of thermal rectification has not been well understood either.

The **objectives** of this study is to investigate thermal transport properties in pristine and functionalized graphene and understand the underlying physics governing the behavior of these properties. The objectives are achieved by using the non-equilibrium molecular dynamics method for atomistic simulation of the graphene material systems, followed by numerical calculations of the physical quantities from the simulation data. We aim to perform atomistic level simulations and theoretical analysis to understand:

1. Effect of size, strain, chirality, and temperature on the thermal transport properties of pristine graphene.
2. Deformation modes of graphene induced by single-side hydrogenation.
3. Thermal conductivity variation in graphene with single-side hydrogenation and its dependence on deformation modes.
4. Thermal conductivity variation in graphene with double-side doping and its dependence on doping stripe coverage and orientations
5. Thermal rectification in graphene with triangular doping pattern.

The rest of the thesis is organized as follows: Chapter 2 describes the methods for the numerical simulation of thermal transport in graphene and the calculation of various related physical quantities; Chapter 3 investigates the thermal transport properties of pristine graphene; Chapter 4 studies hydrogenation induced deformation modes and thermal conductivity variations in graphene; Chapter 5 investigates thermal conductivity variation of graphene with patterned double-size hydrogenation; Chapter 6 discusses our study on the thermal rectification in asymmetrically doped graphene; and conclusions and future work are presented in Chapter 7.

CHAPTER 2 METHOD

Computational modeling and analysis of thermal transport in nanostructured materials is challenging because: (1) the nanostructured materials are inherently complex materials containing multiple chemical ingredients; (2) the description of phonon transport must account a variety of phonon scattering mechanisms along with nano effects (e.g. the dominance of ballistic phonon transport, boundary scattering and interface transmission and reflection of phonons), which could make the physical model extremely complex; and (3) the length scales in nanostructured materials can vary across several orders of magnitude, ranging from few nanometers of the nanoparticle size to millimeters of the size of the bulk structure. As shown in Fig. 1, depending on the characteristic length of the system, a variety of models are available for computational analysis of thermal transport in solid state materials. Along the characteristic length axis, while the models become more sophisticated by taking into account more phonon scattering mechanisms, the model complexity and/or the required computation intensity increase significantly. In

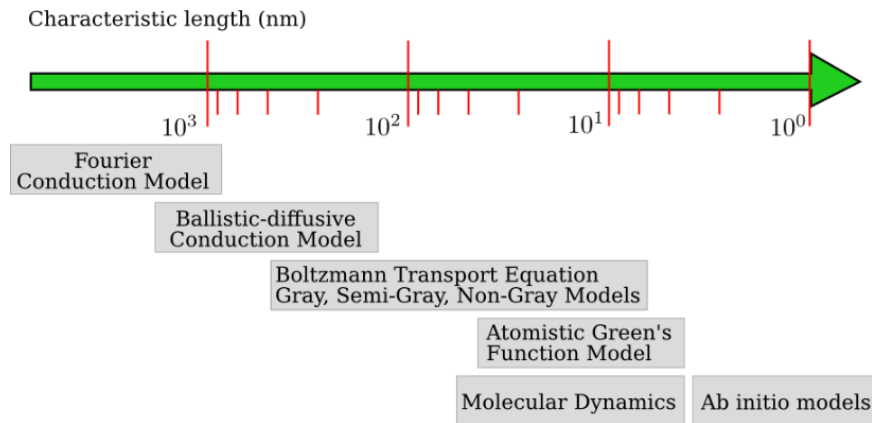


Figure 1: Phonon thermal transport models.

nanostructured materials, when the characteristic length is less than several hundred nanometers, ballistic phonon transport dominates[55]. Interface and boundary scattering play major roles in the thermal resistance of the material[56]. In this case, the diffusive Fourier conduction equation may not be directly applicable. When the characteristic length of the system is comparable or smaller than the phonon mean free path (MFP), phonon Boltzmann transport equation (BTE) based on a particle view of phonon transport can be employed. Within the BTE framework, depending on the level of phonon transport approximation, gray, semi-gray and non-gray models have been developed[55]–[59]. The gray and semi-gray BTE models adopt a frequency-independent relaxation time approximation. The gray BTE model has been used to calculate effective thermal conductivity of 2-D periodic nanocomposites[55]. Although the gray BTE model and its ballistic-diffusive approximation[60] enable efficient calculations of phonon transport, they ignore the wave nature of phonons. The non-gray BTE model combines the wave physics contained in the phonon dispersion curves with BTE’s particle view of phonon transport by taking into account the energy exchange between different phonon modes. However, the non-gray BTE requires detailed local phonon transport properties at different locations in the material which is difficult to obtain for complex material systems. Pure atomistic models such as the molecular dynamics (MD)[61], atomistic Green’s function[62] and *ab initio* models[63] have also been used to compute thermal transport properties of materials. These pure atomistic calculations are typically more accurate as they impose fewer assumptions and simplifications of the system behavior. However, they are computationally more expensive and only suitable for small systems. Due to the size range,

two dimensional structure and the complexity of the graphene system under investigation, for a balanced accuracy and computational cost, we adopt the classical molecular dynamics (MD) approach in this work for the calculations of the thermal transport properties of the graphene systems. As will be described in the following sections, MD offers an effective way to predict the dynamic behavior of nanomaterials by using force fields describing the interactions between atoms. While the direct result from a MD simulation is the movement trajectory of the atoms, material thermal properties such as thermal conductivity and specific heat can be calculated from the displacement and velocity history of the system under properly designed conditions. Furthermore, some of the physical properties such as the phonon dispersion and relaxation times can be obtained through more sophisticated calculations.

2.1 Molecular Dynamics

MD is an atomistic computer simulation technique which utilizes the fundamental laws of classical mechanics to predict the trajectories of atoms or molecules as a function of time. MD utilizes Newton's second law,

$$F_i = m_i a_i, \quad i = 1, 2, \dots, N \quad (2.1)$$

where the subscript i is the atom index and N is the total number of atoms or molecules in a system, m_i is atom mass, the acceleration $a_i = \ddot{r}_i$ and r_i is position vector of atom i , F_i is the force acting on atom i and is obtained from

$$F_i = \frac{\partial V}{\partial r_i} \quad i = 1, 2, \dots, N \quad (2.2)$$

where V is potential energy function. Therefore, the essential part in MD is the calculation of the force F_i . A simulation is accurate only if the calculated forces from the potential are close to the actual interatomic forces. Since the forces are calculated from a given potential, the selection of the potential function plays an important role because the realism of a simulation depends on how well the potential function considered is able to mimic the actual system under given simulation conditions. It should be noted that, although classical MD has been successful in predicting dynamic behavior of nanomaterials, it has several limitations. One major limitation is that the classical approximation is not accurate for studies that involve electrons. Also the number of particles in a system is limited by the computing power available. In addition, at very low temperatures quantum effects become significant.

2.2 Carbon-Carbon Interaction

During the past two decades, many interatomic potentials have been proposed to describe the interactions between the carbon atoms in a lattice [18]. Among them, a recently developed Adaptive Interatomic Reactive Empirical Bond Order (AIREBO) potential [64] has been widely adopted due to its accuracy and generality. In this work, we use the AIREBO potential to describe the interactions between the carbon atoms in graphene. The AIREBO potential is given by

$$V = \frac{1}{2} \sum_i \sum_{j \neq i} \left[V_{ij}^{REBO} + V_{ij}^{LJ} + \sum_{k \neq l, j} \sum_{l \neq i, j, k} V_{kijl}^{TORSION} \right] \quad (2.3)$$

In Eq. (2.3), the term V_{ij}^{REBO} is the second-generation Reactive Empirical Bond Order (REBO) potential developed based on original REBO by Brenner *et al* [65] which describes the interatomic interactions in carbon and hydrocarbon system. It is given by

$$V_{ij}^{REBO} = V_{ij}^R(r_{ij}) + b_{ij} V_{ij}^A(r_{ij}) \quad (2.4)$$

where V_{ij}^R and V_{ij}^A are the repulsive and attractive terms respectively for the pair of atoms i and j . The terms are combined by the bonding term b_{ij} . The quantity r_{ij} is the distance between the i^{th} and j^{th} atoms. The details of the energy repulsive term can be found in Ref.[60] [61]. The term V_{ij}^{LJ} is the Lennard-Jones term that is used describe long range *Van der Waals* interaction between carbon atoms.

$$V_{ij} = 4\epsilon \left[\left(\frac{\sigma}{r_{ij}} \right)^{12} - \left(\frac{\sigma}{r_{ij}} \right)^6 \right] \quad r_{ij} < r_c \quad (2.5)$$

where ϵ is depth of potential well, σ is distance of zero potential, r_{ij} is distance between atom i and atom j , and r_c is cut off distance. In this work, we found that $V_{kijl}^{TORSION}$ can lead to a significant underestimate of graphene. For this reason, it is neglected in the calculations.

MD simulation is able to achieve large size and moderate long simulation time, a benefit from parameterized potential, allowing it to investigate problems like tensile test, heat transport and diffusion. Another important potential is the Tersoff potential [66],

which is a three-body potential that takes into account the environment-dependent bond order to describe strong covalent bonds more accurately. We use Tersoff potential to describe interaction among carbon, silicon and boron atoms. The form of Tersoff potential can be written as,

$$E = \sum_i E_i = \frac{1}{2} \sum_{i \neq j} V_{ij} \quad (2.6)$$

$$V_{ij} = f_C(r_{ij}) [a_{ij} f_R(r_{ij}) + b_{ij} f_A(r_{ij})] \quad (2.7)$$

$$f_R(r_{ij}) = A \exp(-\lambda_1 r_{ij}) \quad (2.8)$$

$$f_A(r_{ij}) = B \exp(-\lambda_2 r_{ij}) \quad (2.9)$$

$$f_C(r) = \begin{cases} 1, & r_{ij} < R - D \\ \frac{1}{2} - \frac{1}{2} \sin \left[\frac{\frac{\pi}{2} (r_{ij} - R)}{D} \right], & R - D < r_{ij} < R + D \\ 0, & r_{ij} > R + D \end{cases} \quad (2.10)$$

$$b_{ij} = (1 + \beta^n \zeta_{ij}^n)^{-1/2n} \quad (2.11)$$

$$\zeta_{ij} = \sum_{k(\neq i,j)} f_C(r_{ik}) g(\theta_{ijk}) \exp(\lambda_3^3 (r_{ij} - r_{ik})^3) \quad (2.12)$$

$$g(\theta) = 1 + c^2/d^2 - c^2/[d^2 + (h - \cos\theta)^2] \quad (2.13)$$

$$a_{ij} = (1 + \alpha^n \eta_{ij}^n)^{-1/2n} \quad (2.14)$$

$$\eta_{ij} = \sum_{k(\neq i,j)} f_c(r_{ik}) \exp[\lambda_3^3 (r_{ij} - r_{ik})^3] \quad (2.15)$$

where i, j, k are indexes of atoms, total potential E is sum of pairwise potential V_{ij} , r_{ij} is bond length between i th atom and j th atom, θ_{ijk} is bond angle between ij and ik . The functions f_R and f_A represent repulsive and attractive potential respectively. The bond order parameter b_{ij} determines the bond length by considering distance, coordination and bond angle. Function ζ_{ij} represents an angle dependent bond counter within the cutoff [67].

Time integration algorithm in MD simulation is used to integrate equation of motion to update particle trajectory. Based on finite difference methods, time integration algorithm takes position, velocity and acceleration at time t and calculates these quantities at later time. The Verlet algorithm is a simple, accurate, fast, and widely used time integration algorithm in MD simulation. The position, r , at the next time step is written as,

$$r(t + \Delta t) = 2r(t) - r(t - \Delta t) + a(t)\Delta t^2 + O(\Delta t^4) \quad (2.16)$$

where the acceleration $a(t) = -\left(\frac{1}{m}\right) \nabla V(r(t))$, m is mass of the atom. The truncation error is of order of Δt^4 . Velocity Verlet [68] is Verlet-like algorithm that gives velocities in a more straightforward way,

$$r(t + \Delta t) = r(t) + v(t)\Delta t + \frac{1}{2}a(t)\Delta t^2 \quad (2.17)$$

$$v(t + \Delta t) = v(t) + \frac{1}{2}[a(t + \Delta t) + a(t)]\Delta t \quad (2.18)$$

With the interatomic potential defined, the Velocity Verlet is used with a time step chosen to integrate the equation of motion. The chosen time step is based on the motion of lightest atoms and computational cost.

2.3 Thermal Conductivity

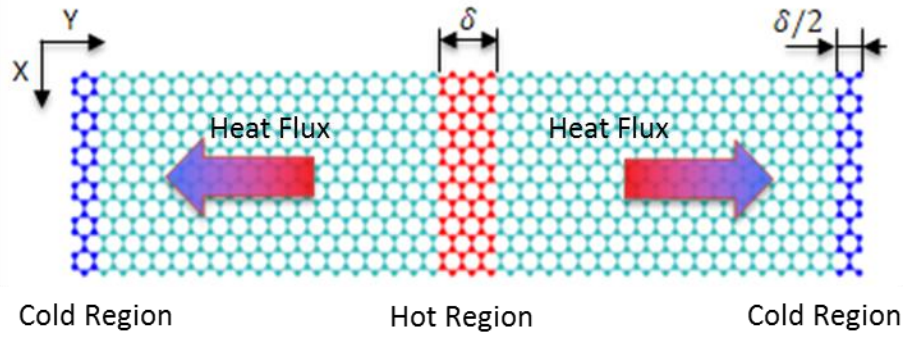


Figure 2: Schematic diagram of a graphene sheet for the calculation of thermal conductivity. The graphene sheet has one cold region (blue), two heat flux regions (green) and one hot region (red).

There are two common methods in MD to calculate thermal conductivity. The Green-Kubo and the direct method [69]. The Green-Kubo method, based on fluctuation-dissipation theory, uses the autocorrelation of heat flux to calculate thermal conductivity. The direct method generates a heat flux in non-equilibrium molecular dynamics by switching the high and low kinetic energies in two prescribed regions in the material, making one “hot” and the other “cold”, as shown in Fig. 2.

Along the heat flux direction, a temperature profile is formed with temperature decreasing from hot to cold region. In the non-equilibrium MD simulation of graphene, along the heat flux direction, the graphene sheet is divided into bins with the width of

$\sqrt{3}a/2$, where $a = 1.42 \text{ \AA}$ is the lattice constant of graphene. The temperature profile can then be calculated by averaging the kinetic energy of each bin as

$$T_i = \frac{1}{3N_i k_B} \sum_{j=1}^{N_i} m v_j^2 \quad (2.19)$$

where T_i is the temperature of the i -th bin, N_i is the number of carbon atoms in the i -th bin, k_B is Boltzmann's constant, m is the mass of carbon atom and v_j is the velocity of atom j . Meanwhile, the heat flux q is obtained as

$$q = \frac{\Delta E}{2At_s} \quad (2.20)$$

where A is the cross-sectional area of heat flux region with the thickness of 3.4 \AA , t_s is the time period taken for statistical averaging after the non-equilibrium steady state of the system is reached, ΔE is the total swap energy during t_s . Thermal conductivity can be calculated using the Fourier's Law as,

$$q = -k \nabla T \quad (2.21)$$

where q is the heat flux, k is the thermal conductivity and ∇T is the temperature gradient. Both Green-Kubo and direct method give a good estimation of thermal properties. However, Green-Kubo method requires a long convergence time for heat flux correlation function and is more desirable in homogeneous system such as perfect crystalline materials [70]. The direct method is preferable in studying inhomogeneous system, such as graphene with doping patterns.

2.4 Phonon Density of States

Energy carriers in solid-state materials are electrons and phonons. In graphene, phonon is the major contributor to heat conduction and electron contributes very little, according to the Wiedemann-Franz law that estimates the thermal conductivity caused by electron [71]. Phonons are quantized energies in the vibrational modes of the material lattice. The quantum of the vibrational energy of a given vibrational mode is called a phonon. Phonons can be treated as particles with energy and momentum. The energy of a phonon can be written as $E = \hbar\omega$, where \hbar is the Planck's constant and ω is the frequency of a given vibrational normal mode of the lattice. The energy density distribution along the frequency axis of a lattice is represented by the phonon density of states (PDOS). The PDOS is an important quantity to characterize atomic vibration and estimate the thermal transport properties of the material. PDOS can be calculated through the Fourier transformation of the velocity auto-correlation function as,

$$D(\omega) = \int \langle \mathbf{v}(t) \cdot \mathbf{v}(0) \rangle e^{-i\omega t} dt \quad (2.22)$$

where $D(\omega)$ is the PDO, \mathbf{v} is the atomic velocity, and the angle bracket represents autocorrelation function.

2.5 Specific Heat

In order to thoroughly understand the relation between thermal conductivity variation with the doping coverage and doping stripe orientation, we rewrite the thermal conductivity definition based on the kinetic theory of the lattice thermal transport as

$$\kappa = \frac{1}{3} \sum_{v=1}^{3n} C_V v_v^2 \tau_v = \frac{1}{3} \sum C_V v_v \Lambda_v \quad (2.23)$$

where C_V is the specific heat, v_v is the phonon group velocity, τ_v is phonon relaxation time, and Λ_v is the phonon mean free path (MFP). The subscript v denotes the phonon mode (\mathbf{k}, ω) , where \mathbf{k} is the wave vector and ω is the angular frequency. With the unit of joule per mole kelvin, the specific heat, C_V , can be calculated based on the PDOS as[72][73][74],

$$\begin{aligned} C_V &= \frac{k_B}{m_L} \int_0^{\omega_{max}} \left(\frac{\hbar \omega}{k_B T} \right)^2 \frac{e^{\frac{\hbar \omega}{k_B T}}}{\left(e^{\frac{\hbar \omega}{k_B T}} - 1 \right)^2} g(\omega) d\omega \\ &= \frac{k_B}{m_L} \int_0^{\omega_{max}} Y(\omega, T) g(\omega) d\omega \end{aligned} \quad (2.24)$$

where $g(\omega)$ is the PDOS, \hbar is the Plank's constant, m_L is the mole amount of the atoms in the system and k_B is the Boltzmann constant.

2.6 Spectral Energy Density

We integrate the spectral energy density (SED) method with our MD simulation to evaluate the anharmonic phonon properties of the carbon atoms in the hydrogen doping graphene, including the relaxation time and phonon group velocity. In addition, phonon dispersion relation obtained from SED is reliable as it uses information directly obtained from real-time MD simulations which already include anharmonic and temperature effects [75]. N -phonon scattering, normal and Umklapp scattering are all included in the

simulation results. In order to calculate phonon SED, we first define the SED unit cell as the smallest group of atoms repeating along the heat flux direction. Derived from the time derivative of normal modes, the phonon SED can then be expressed as a function of angular frequency ω and wave vector \mathbf{k} as [76]

$$\Phi(\mathbf{k}, \omega) = \frac{m_j}{2\pi t_0 N_l} \sum_{\alpha}^3 \sum_j^{N_j} \left| \int_0^{t_0} \sum_l^{N_l} \dot{u}_{\alpha}(jl, t) e^{i\mathbf{k} \cdot \mathbf{r}_0^l} e^{-i\omega t} dt \right|^2 \quad (2.25)$$

where $\dot{u}_{\alpha}(jl, t)$ is the velocity of j -th atom in the l -th SED unit cell at time t , α represents velocity direction (in x, y and z), \mathbf{r}_0^l is the equilibrium position of l th unit cell, m is the mass of carbon atom, N_j is number of atoms in the SED unit cell and N_l is the number of SED unit cells. The wave vector \mathbf{k} is in direction from Γ point to K point, which is corresponding to zigzag graphene direction in real space. The resolution of wave vector \mathbf{k} is based on the number of SED unit cell along the heat flux direction. The wave vector \mathbf{k} is discretized as $k_n = \frac{2\pi n}{aN_l}$, $n = 0, 1, 2, \dots, N_l - 1$, where a is lattice constant. Here it is discretized into $N_l/2$ points ranging from 0 to π/a with a as the lattice constant. Velocity profile of each carbon atom is collected under NVE ensemble with equilibrium state. We are able to generate the SED function with high resolution in frequency domain by using the velocity profile of carbon atom within 100 ps time period. For j -th atom in the SED unit cells, a matrix of atomic velocities $\dot{u}_{\alpha}(jl, t)$ in α -direction is established such that the column index represents the unit cell number l and the row index represents the discrete time instances t . Each column delivers velocity histogram of the j -th atom in the l -th SED unit cell. The Fourier transformation of this matrix yields the spectral energy density of j -

th atom in the SED unit cells. $\Phi(\mathbf{k}, \omega)$ is obtained as the sum of the spectral energy density of all the atoms in the SED unit cells in all three directions. In discrete Fourier transform, n in k_n is ranging from 0 to $N_l - 1$, which can be mapped into the value of wave vector ranging from 0 to $\frac{2\pi}{a_u}$. Since $\Phi_{k,\omega}$ is symmetric about the center, we take half of N_l . Thus, the dispersion interval is from $k=0$ to $k=\frac{\pi}{a_u}$.

2.7 Phonon Relaxation Time

In a classical harmonic system, the relaxation time is infinite. In an anharmonic system such as the graphene lattice described by the AIREBO potential, phonon populations fluctuate according to the equilibrium distribution function [77]. In each normal mode, phonons are being created and destroyed simultaneously. The phonon population number n is proportional to Q^*Q , where Q is the normal mode amplitude. The finite phonon relaxation time can be estimated through the decaying normal-mode amplitudes as [78]

$$\tau = \frac{\int_0^\infty \langle \delta n(t) \delta n(0) \rangle dt}{\langle (\delta n)^2 \rangle} \quad (2.26)$$

where τ is the phonon relaxation time, δn is the fluctuation of n from its equilibrium state. Relaxation time can also be derived from phonon line-width in the frequency domain since phonon density of states shows the vibration spectrum with peaks being shifted and broaden due to the anharmonic interactions [79]. The relation of phonon relaxation time and phonon line-width is given by,

$$\tau = \frac{1}{2\Gamma} \quad (2.27)$$

where τ is the phonon relaxation time and Γ is the phonon linewidth. It can be shown that kinetic energy can be written as [80],

$$T(\mathbf{k}, \nu, t) = \frac{1}{2} \lim_{\tau_0 \rightarrow \infty} \frac{1}{2\tau_0} \int_{-\tau_0}^{\tau_0} \dot{Q}^*(\mathbf{k}, \nu, t) \dot{Q}(\mathbf{k}, \nu, t) dt \quad (2.28)$$

where \dot{Q} is the derivative of normal mode amplitude. The kinetic energy can be transformed into frequency domain using Parseval's theorem [81]. Following the derivation in Ref. [76], we obtain another form of the SED equation as,

$$\Phi(\mathbf{k}, f) = \sum_{\nu}^{3n} \frac{C(\mathbf{k}, \nu)}{[4\pi\tau(f - f_0(\mathbf{k}, \nu))]^2 + 1} \quad (2.29)$$

where \mathbf{k} is the wave vector, f is the frequency, $f_0(\mathbf{k}, \nu)$ and $C(\mathbf{k}, \nu)$ are the peak frequency and magnitude for the phonon branch denoted by ν , and τ is the phonon relaxation time. The new SED equation is expressed as the sum of the Lorentzian functions of all $3n$ phonon branches. Hence, by fitting the spectral energy density to a Lorentzian function, the corresponding relaxation time of phonons, $\tau(\mathbf{k}, f)$, can be evaluated.

CHAPTER 3 THERMAL TRANSPORT PROPERTIES OF PRISTINE GRAPHENE

In this chapter, we calculate the thermal conductivity of pristine graphene and investigate the size, strain, chirality and temperature effect on the thermal transport properties. There are three purposes for these investigations: (1) to validate the computational approach for obtaining the thermal transport properties of graphene; (2) to obtain reference thermal transport properties (i.e. property values of pristine graphene; and (3) to investigate and identify the material parameters and extremal conditions that can have a significant effect on the thermal conductivity.

3.1 Size Effect on Thermal Conductivity of Pristine Graphene

It is well known that size plays an important, sometimes dominant, role in the thermal conductivity of nanomaterials. This is due to the ballistic phonon transport and significant boundary scattering in the nanomaterials. When the size of the material is smaller than the mean free path of phonon-phonon scattering, the phonon transport becomes more ballistic. In this case, the boundary of the materials becomes a major source for phonon scattering, and the overall phonon mean free path is largely determined by the boundary-to-boundary distance which is the size of the material. As shown in Eq. (2.23), the phonon mean free path is directly related to the thermal conductivity of the material. In this section, we study the size effect on graphene TC by changing width and length of graphene. It should be noted that, periodic boundary condition is applied in the width (vertical) direction of the graphene to represent a graphene that is very large in the width

direction. However, even with the periodic boundary condition, the width of the graphene cannot be too small in NEMD simulations due to the “simulation box” effect. To determine the minimum width for our simulations, different widths (with constant length = 19.6 nm and 19.8 nm for zigzag and armchair graphene) are used in the MD simulations and the TC is computed. It is shown in Fig. 3(a) that the value of TC converges to a constant value when the simulation width is larger than 5 nm. Therefore, when a periodic boundary

condition is applied in the width direction, the width of the simulation box is taken to be 5 nm. On the contrary, the TC changes significantly with length as the length of the simulation box represents the real length of the graphene in the heat flux direction. Figure 3 (b) shows the result of graphene TC with different lengths and a constant width of 5 nm. TC decreases rapidly with decreasing length from 200 nm to 10 nm. Note that, the values here are much lower than the experimental results of the bulk graphene[82], which is in the range of 3000-5000 W/mK. This is

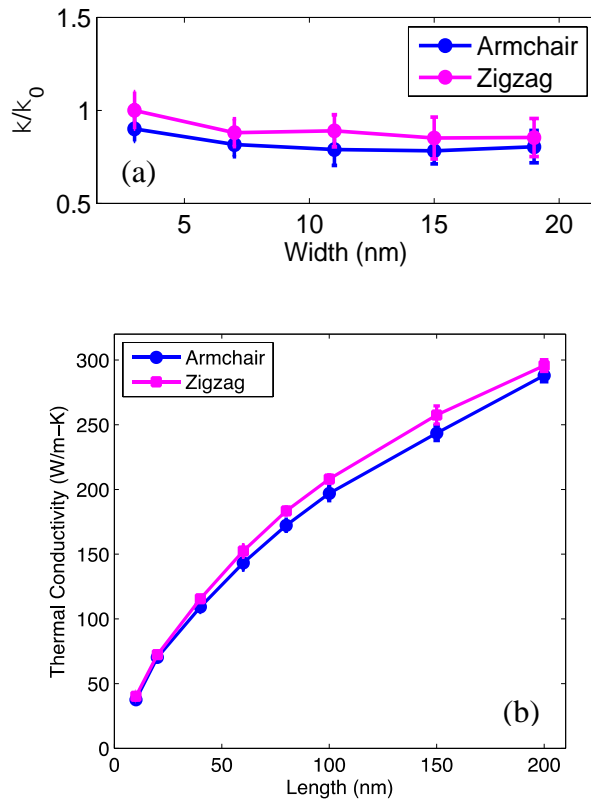


Figure 3: Size effect of thermal conductivity. (a) TC variation as a function of width (length = 19.8 and 19.6 nm for armchair and zigzag graphene, respectively), (b) TC variation as a function of length (width = 4.9 and 5nm for armchair and zigzag graphene, respectively).

due to the fact that the simulation box is much smaller than the bulk MFP which is about 775 nm at room temperature, in which case the thermal transport is dominated by Umklapp phonon-phonon scattering and thus diffusive. In the MD simulations performed in this work, long wave length phonons are cut-off by the simulation box and boundary scattering of phonons dominates in this ballistic regime. It is worth noticing that the TCs of armchair and zigzag graphene are close, indicating that pristine graphene is nearly isotropic in heat transfer.

3.2 Strain Effect on Thermal Conductivity of Pristine Graphene

While the size effect on the thermal conductivity of graphene is well-known and is investigated in Section 3.1 using NEMD simulations, strain effect, which falls in a broader category of mechanical effects, has not attracted much attention in the design of graphene based systems. Computational analysis of strain effect on the phonon thermal conductivity could introduce additional dimensions to the design space of graphene structures for various applications. In this section, we investigate the strain dependence of thermal conductivity in both armchair and zigzag graphene. A uniaxial strain is applied to the pristine graphene in the longitudinal direction at the rate of 0.001 /ps while maintaining zero stress in transverse direction with temperature at 300K under the NPT ensemble. Periodic boundary conditions are applied in the width direction. Graphene is in a ripple structure after relaxation. It returns to the planar mode with tensile strain and forms a corrugated surface with compressive strain. We calculate TC with different strains using the NEMD method and normalized the values by dividing κ_0 which is the TC of zigzag graphene with no strain applied. As shown in Fig. 4, graphene TC decreases slightly with

compressive strain. However, it is much more sensitive to tensile strain. The TC decrease as much as 40% and 15% in armchair and zigzag graphene, respectively, when the tensile strain = 0.1. Due to the unique 2D structure, graphene in compression undergoes virtually no changes in bond angle and bond length, which means there is little change in the atomic force, and most of the deformation is due to rigid body rotation of the bonds. The strain dependence of TC can be understood by the calculated PDOS shown in Fig. 5. The numbers beside the PDOS curves represent the corresponding strains. It is shown that compressive strain does not alter the PDOS while tensile strain causes a red-shift of G-band in PDOS, resulting in a decrease of phonon group velocity of all branches. According to the classical lattice thermal transport theory shown in Eq. (2.23), TC is proportional to the phonon group velocity. Graphene TC decreases as the group velocity becomes slower. In addition, although optical modes carry very small heat, a downward shift of the optical phonons can

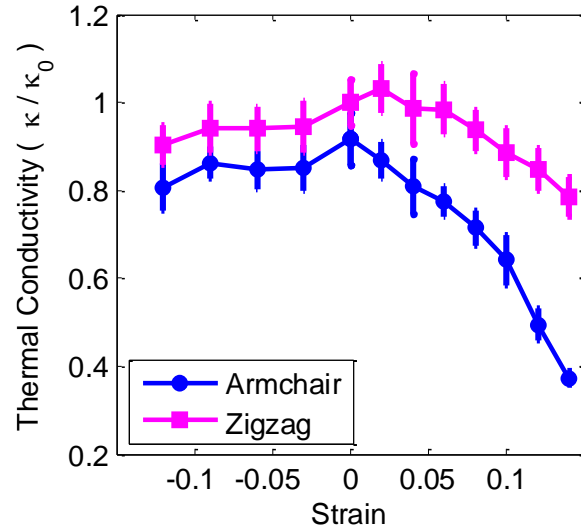


Figure 4: Thermal conductivity of graphene with tensile and compressive strain.

affect thermal transport significantly since it becomes easier for them to scatter with acoustic phonons[83].

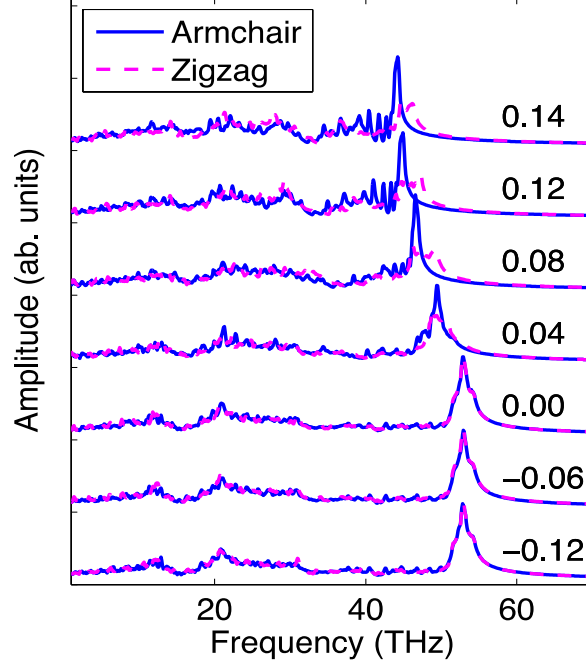


Figure 5: Phonon density of states for graphene under tension and compression.

Another observation we have made is the appreciable TC difference between the armchair and zigzag graphene when they are under tensile strain. The TC in armchair graphene drops much faster than that in zigzag graphene. This behavior can be explained, at least partially, by the red shift of the G-band. As shown in Fig. 5, there is a significant difference of the G-band red shift in the two types of graphene. When the strain is higher, the optical band shift in the armchair graphene is more than that in the zigzag graphene, indicating more scattering between the optical and acoustic phonons in the armchair graphene.

3.3 Temperature Effect on Thermal Conductivity of Pristine Graphene

Another important factor that can affect TC is temperature. In this section, we examine the temperature effect on thermal transport in pristine graphene. The graphene features three different lengths: 19.6 nm, 39.2 nm and 998.9 nm with temperature varying from 300 K to 1000 K. As shown in Fig. 6, the TC of the short graphene (length = 19.6 nm) changes little with the temperature increase while there is a large decrease of 20% and 30% in TC of the intermediate (length equals 39.2 nm) and long (length=998.9 nm) graphene sheets, respectively, as temperature increases from 300K to 1100K.

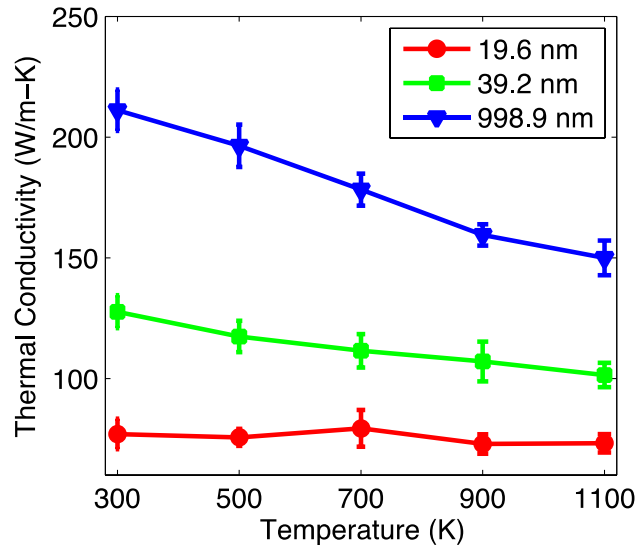


Figure 6: Variation of thermal conductivity of graphene as a function of temperatures.

As discussed in Section 3.1, for single crystal perfect nanomaterials, there are two scattering mechanisms that impedes phonon transport: boundary scattering and Umklapp phonon-phonon scattering. According to Matthiessen's rule of the phonon mean free path (MFP),

$$\frac{1}{\Lambda} = \frac{1}{\Lambda_b} + \frac{1}{\Lambda_{p-p}} \quad (3.1)$$

Where Λ is the effective phonon MFP, Λ_b is the MFP limited by material boundary, Λ_{p-p} is the MFP of the Umklapp phonon-phonon scattering. At room temperature, Λ_{p-p} of bulk graphene is about 775 nm. When the graphene size is smaller than 39.2 nm, the term $1/\Lambda_b$ is much larger than $1/\Lambda_{p-p}$. The effective phonon MFP is determined by Λ_b . Therefore, the boundary scattering dominates the phonon scattering. Although Λ_{p-p} decreases as the temperature increase, such reduction in Λ_{p-p} has little effect on the effective phonon MFP since in this case boundary scattering is the dominant term in Eq. (3.1). For this reason, the TC hardly changes with temperature. However, when graphene size is comparable or larger than Λ_{p-p} , the term $1/\Lambda_b$ becomes comparable to $1/\Lambda_{p-p}$. In

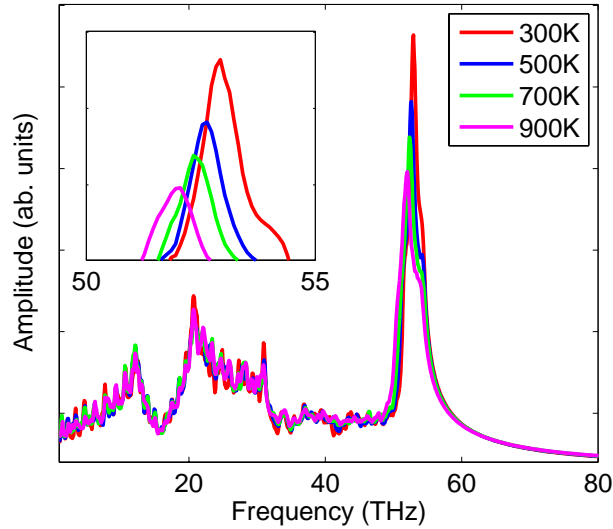


Figure 7: Normalized PDOS of graphene at different temperatures, size = 5 nm × 39.2 nm.

this case, the temperature effect on Λ_{p-p} is reflected on the effective MFP Λ . Therefore, TC decreases with temperature increase. As shown in normalized PDOS in Figure 7, temperature dependence of thermal conductivity can also be explained by the down shifting of the G-band of PDOS as temperature increasing, which indicates an enhancement of phonon-phonon scattering as well as a decrease of phonon group velocity.

CHAPTER 4 HYDROGENATION INDUCED DEFORMATION MODE AND THERMAL CONDUCTIVITY VARIATIONS IN GRAPHENE SHEETS

In this chapter, we investigate thermal transport tuning of graphene through chemical functionalization. We demonstrate controllable thermal conductivity tuning through patterned hydrogenation of graphene. We perform non-equilibrium molecular dynamics (MD) studies of hydrogenated graphene and show that single-sided patterning of hydrogen on relaxed graphene produces global deformation modes due to the local stress caused by sp^3 C–C bonding. Such deformation modes can be controlled by the hydrogenation patterning parameters. Furthermore, first principles theory calculations are performed to elucidate the relation between the deformation modes and local stress induced by patterned hydrogenation. We show that both the doping density and deformation mode contribute to the thermal conductivity variation of the graphene sheet. Our results demonstrate that, with the control of hydrogenation patterning parameters, desired deformation mode and thermal conductivity of graphene can be achieved for applications such as thermoelectric energy conversion or foldable electronics.

4.1 Simulation details

In carbon materials, such as graphene, heat conduction by phonons is dominant due to the strong covalent sp^2 bonding between carbon atoms. In nanoscale, k is closely related to size, boundary conditions and geometry of the atomistic structures due to the ballistic transport of phonons and significant or even dominant phonon-boundary scattering. Previous studies have shown that thermal conductivity of graphene has significant size

dependence and increases quickly with the increasing length along the heat flux direction.[84][23] The thermal conductivity of graphene nanoribbon decreases remarkably with tensile strain[85][86] and defects.[24][87] Effect of hydrogenation on the thermal conductivity of graphene has also been investigated. It has been shown that random hydrogenation or edge hydrogen passivation will bring a rapid drop of the graphene's thermal conductivity.[36][37][88] The thermal conductivity's reduction path is closely related with the direction of the patterned hydrogenation stripes, but not significantly related with the heat flux direction.[89] Different from these studies, the single-sided hydrogenation patterning considered in this work brings morphology of graphene into the thermal transport tuning, resulting in fundamentally different characteristics of the thermal conductivity variation compared to those of random or edge hydrogenation.

Non-equilibrium molecular dynamics simulations are performed by using the molecular dynamics solver LAMMPS[90] as described in Chapter 2. Although an optimized Brenner empirical potential has been recently proposed for better approximation of thermal conductivity of graphene [91], we adopt the adaptive intermolecular reactive empirical bond order (AIREBO) potential with REBO and Lenard Jones terms to describe the short range and long range of C-C, C-H interactions [22][92] for the following reasons: (1) the deformation modes predicted in this study require validated approximation of graphene's mechanical properties, which have not been well tested with the optimized Brenner potential; and (2) the torsional term of the AIREBO potential is not included as it causes significant underestimation of the thermal conductivity of graphene. The graphene

sheet is decomposed into cold, hot, and heat flux regions along the zigzag direction as shown in Figure 2. The length of cold, hot and each of the heat flux regions are 5%, 5% and 45% of the graphene sheet length, respectively. Periodic boundary condition (PBC) is applied to the simulation box with a 5nm thick vacuum space perpendicular to the graphene sheet in order to prevent the non-bonding long range interaction. With a time step of 0.5fs, the graphene sheet is first relaxed to the equilibrium state at 300K for 50ps under the isothermal isobaric ensemble (NPT). Next, with the microcanonical ensemble (NVE), a heat flux is imposed on the system by exchanging the velocity of the lowest kinetic energy atom in the hot region with the velocity of the highest kinetic energy atom in the cold region. After reaching the non-equilibrium steady state, the exchanging process continues for $t_s = 100\text{ps}$ in order to calculate the thermal conductivity. Along the heat flux direction, we divide the graphene sheet into bins with the width of $\frac{\sqrt{3}}{2}a$ where $a = 1.42\text{\AA}$ is the lattice constant. The temperature profile can be calculated by averaging the kinetic energy of each bin using Eq. (2.19). Meanwhile, the heat flux q is obtained by using Eq. (2.20). Then, the thermal conductivity can be calculated by using Eq. (2.21). To help elucidate the effect of phonon spectrum on the thermal transport, we calculate phonon density of states (PDOS) through the Fourier transformation of the velocity auto-correlation function as shown in Eq. (2.22). After reaching the steady state, the total time period considered for PDOS calculation is 10ps.

As a validation of the simulation method described above, we first calculate the thermal conductivity of pristine graphene as a function of size. It is found that thermal

conductivity increases significantly with the increasing length of the heat flux region because of the maximum phonon wavelength the system can carry is closely related to the heat flux length and the periodic boundary condition that has been applied. However, the size effect perpendicular to the heat flux direction is negligible. These simulation results are quite close to those presented in Ref. [23][22]. For the sake of brevity, they are not shown here. In the following simulations, the graphene sheet size is defined as $5.10\text{nm} \times 19.65\text{nm}$ with the PBC along the two in-plane directions.

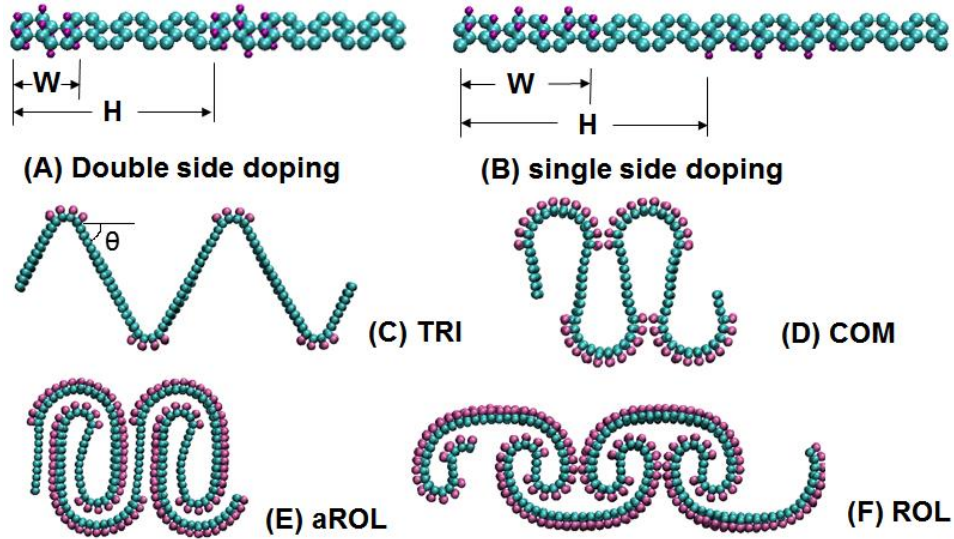


Figure 8: (color online) (A) schematic diagram of patterned double-side hydrogenation; (B) schematic diagram of patterned single-side hydrogenation; (C-F) deformation modes induced by patterned single-side hydrogenation: (C) TRI mode, (D) COM mode, (E) aROL mode and (F) ROL mode.

It has been found that thermal conductivity of graphene greatly depends on the hydrogenation pattern and coverage[36]. In this study, with the consideration of the flexibility of graphene as a two dimensional material, we show that the morphology of

graphene can be manipulated by the hydrogenation pattern. We investigate two types of hydrogenation pattern: double-side doping and single-side doping. Double-side hydrogenation means that in identical hydrogenation-graphene stripes, hydrogen atoms are bonded on both sides of the graphene lattice in an alternative fashion, as shown in Fig. 8(A). The doping density is defined as the ratio of hydrogenation length W to stripe length H , i.e., W/H . We apply two hydrogenation-empty stripes perpendicular (transverse stripes) and parallel (longitudinal stripes) to the heat flux direction, respectively, and vary the doping density. We observe that with the double-side hydrogenation stripes, the relaxed graphene sheet remains planar with a rippling structure.

4.2 Deformation Mode Induced By Single-Side Hydrogenation

Next we consider a single-side hydrogenation pattern with identical hydrogenation-graphene stripes perpendicular to the heat flux direction as shown in Fig. 8(B). The definition of W , H and doping density are the same as in the double-side hydrogenation case. In this study, we investigate four cases with 4, 6, 8 and 10 transverse stripes along the zigzag direction of the graphene with W equal to 4.91nm, 3.27nm, 2.46nm and 1.96nm, respectively. We observe that the relaxed graphene structure no longer remains planar due to the local stress concentration induced by the patterned hydrogenation. Depending on H and W/H ratio, the graphene sheet can be relaxed to the following deformation modes: triangular mode (TRI), compact mode (COM), asymmetric rolling mode (aROL) and symmetric rolling mode (ROL), as shown in Fig. 8(C-F). The TRI mode includes symmetrically bent hydrogenation regions and planar undoped graphene regions.

As depicted by the filled symbols in Fig. 9(A), the slope of the planar graphene regions, θ , is linearly proportional to the hydrogenation length W , and independent of the stripe length H . The COM mode appears when the bending slope of the hydrogenation region is over 90° or $W > 0.65\text{nm}$, where the inter-layer long range interaction between graphene segments starts to play a role. If H is sufficiently large ($> 45\text{nm}$), further increasing W would cause the graphene deform into an unstable asymmetric mode (Fig. 8(E)) with the ratio $0.7 < W/H < 0.8$, and a stable symmetric mode (Fig. 8(F)) with a higher ratio of W/H .

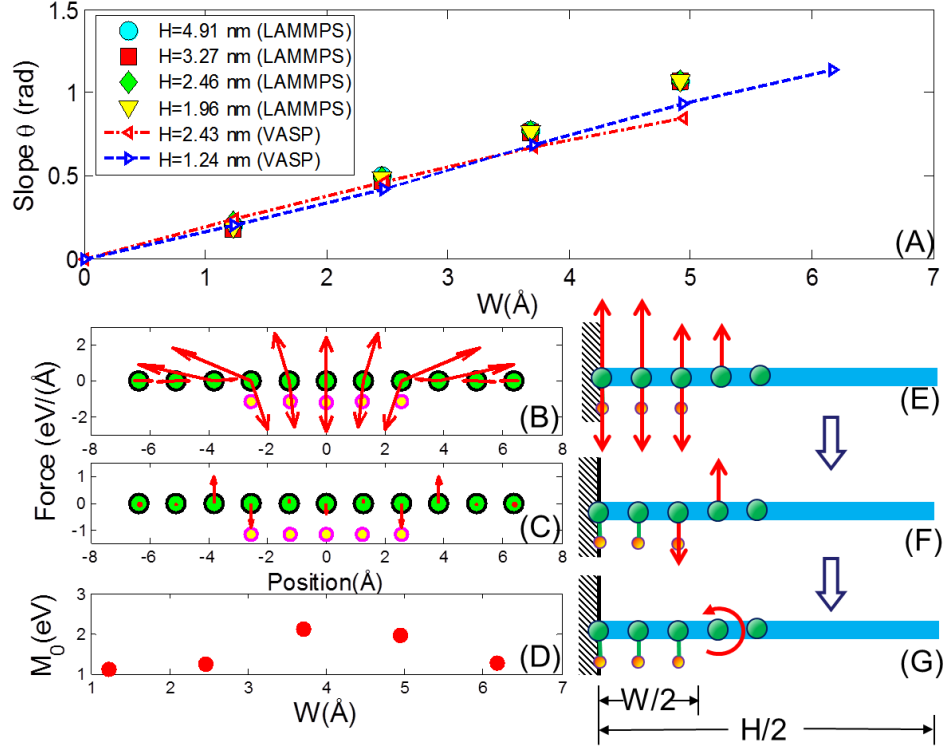


Figure 9: (color online) (A) slope q variation with hydrogenation length W ; (B-G) schematic diagrams of the beam bending model (E, F, G) with the corresponding force and moment calculated from the first principles theory (B, C, D).

In order to fully understand the relation between the slope θ and the length W of the hydrogenation region in the TRI mode, we perform first principles theory calculation with the Vienna ab initio simulation package (VASP).[93][94] The electron-ionic core interaction is represented by the PAW pseudopotential and the electron exchange and correction is treated by Perdew Burke Ernzerhof (PBE)[95] formulation. The cutoff energy for the plane-wave is 500eV. Along the out of plane direction, a vacuum region of 5nm is applied on each side of the sheet in order to eliminate the interaction between the graphene layers. A K-point mesh of $3 \times 3 \times 1$ is used with the Monkhorst-Pack sampling scheme. The width of the supercell is 4.62Å along the armchair direction. The length of the supercell varies from 24.60Å to 49.192Å, along the zigzag direction. Two stripes are considered in each supercell as shown in Fig. 8(B). The bond length is relaxed to be 1.42Å. We first fix the graphene sheet and relax the hydrogen atoms in order to calculate the local forces due to the sp^3 C-C bonding. Then we fully relaxed the structure so that various deformation mode can be observed. Same as the molecular dynamics simulation, the TRI mode is observed with low W/H ratio. The linear relation between the bending slope q and the hydrogenation length W is shown as the dash lines in Fig. 9(A). The slope variations match between first principles theory calculations and molecular dynamics simulations.

To elucidate how the bending deformation of the graphene is induced by the hydrogenation within the stripe, we employ a super cell of 4.62Å×49.19Å with $W = 7.38$ Å as an example to plot the force distribution on carbon atoms as shown in Fig. 9(B). Each

green circle represents two carbon atoms along the width of the supercell. Each pink circle represents one hydrogen atom bonded with the carbon atom next to it. The red arrows represent the force acting on each of the carbon atoms. Figure 9(C) shows the net force along out of plane direction per unit width (4.62\AA). It is clearly shown that a force couple appears at the boundary of the doped region. As shown in Fig. 9(E-G), considering the symmetry of the deformation, the half of the hydrogenation region can be represented as a one-dimensional cantilever beam subject to a constant bending moment M_0 at a distance $W = 2$ from the fixed end of the beam. The bending moment is obtained from the ab initio calculation as $1.54 \pm 0.46\text{eV}$ (Fig. 9(D)). For the cantilever beam, the relation between the bending slope θ and the length of the beam can be obtained from classical mechanics as $\theta = M_0 W / 2EI$, where M_0 is the bending moment and EI is the bending rigidity. The slope equation clearly shows that the slope θ is linearly proportional to the hydrogenation length W and independent of the beam length H . In our calculation, $\partial\theta/\partial W = 0.62 \pm 0.06$ (rad/nm). The bending rigidity EI can be derived as $4.97 \pm 1.59\text{eV}\cdot\text{\AA}$.

4.3 Thermal Conductivity Variation with Double-Side Hydrogenation Stripes

With double-side hydrogenation patterns, we calculate the effective thermal conductivity of the hydrogenated graphene by defining the temperature gradient as $(T_{max} - T_{min})/L$ where T_{max} , T_{min} and L are the highest temperature, lowest temperature and length between T_{max} and T_{min} , respectively. With longitudinal and transverse double-side hydrogenation patterns, Fig. 10(A, B) show the thermal conductivity variation as a function of doping coverage and the PDOS under various doping coverage, respectively. With the increasing of the doping coverage, the thermal conductivity shows a decreasing

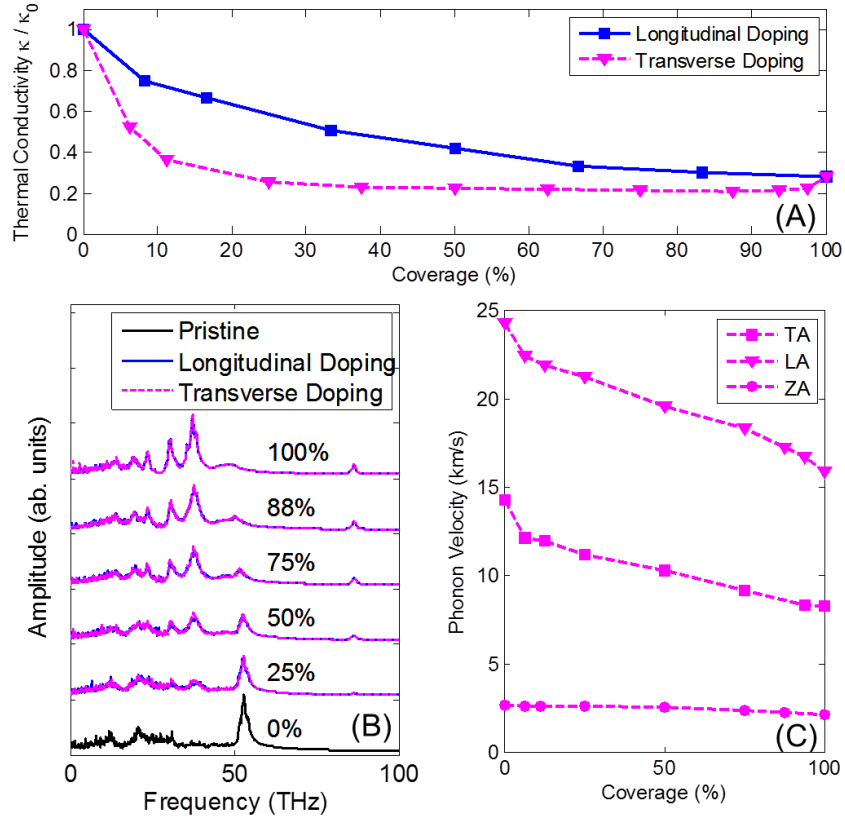


Figure 10: (A) Thermal conductivity variation as a function of doping coverage with longitudinal and transverse hydrogenation patterns; (B) PDOS under various doping coverage conditions with longitudinal and transverse hydrogenation patterns; (C) Acoustic phonon velocity variation as a function of the transverse doping coverage.

trend. Zero coverage of hydrogenation represents pristine graphene. The phonon dispersion curve of pristine graphene [96] indicates that the highest peak region (G-band) of the PDOS contains optical phonons. The PDOS region immediately to the left of the G-band contains the longitudinal acoustic phonons at the Brillouin zone boundary. A red shift (shift to the left) or a decay of the G-peak simultaneously represents a lowering of the longitudinal acoustic phonon dispersion curve. Thus, the red shift of G-peak implies a reduction of the phonon velocity. Graphene with 100% coverage of hydrogenation is called graphane. Compared to graphene, the phonon dispersion of graphane [97] indicates a downward shift of the dispersion curves and a split of the longitudinal acoustic and optical phonon bands. With the PDOS in Fig. 10(B), it is clear that when the hydrogen coverage increases, (1) acoustic phonon dispersion curves are lowered; and (2) phonons are redistributed among the bands. From our MD simulations of graphene sheet with transverse hydrogen doping, we have calculated the phonon velocities of the in-plane longitudinal (LA), in-plane transverse (TA) and out-of-plane (ZA) phonon velocities as shown in Fig. 10(C). It shows a reduction in LA velocity as the hydrogen coverage increases. TA velocity also decreases, although more slowly. The ZA velocity remains mostly the same. Note that, at 300K, the specific heat capacity is relatively insensitive to the decay of the G-band [98]. In addition, it is well known that hydrogenation reduces the phonon mean free path of graphene. Thus, the reduction of the thermal conductivity of double-side hydrogenation can be attributed to the combined effect of reduced phonon velocity and reduced phonon mean free path.

Although the PDOS are similar for longitudinal and transverse doping patterns, the thermal conductivity variation with doping coverage are different, which is due to the doping direction. The longitudinal hydrogen doping only reduces the coverage of sp^2 C–C bonding without interrupting the phonon transport path along the heat flux direction. The thermal conductivity gradually decreases with the increasing of hydrogen coverage. However, the transverse hydrogen doping creates transverse barriers with sp^3 C–C bonding and reduces the phonon mean free path in the heat flux direction, causing a large reduction in the thermal conductivity even at a small hydrogen coverage. When the coverage increases beyond 85%, the transition thermal resistance regions of the two neighboring hydrogenation boundaries start to overlap and diminish when the coverage approaches 100%, resulting a small increase of thermal conductivity as shown in Fig. 10(C).

4.4 Thermal Conductivity Variation with Double-Side Hydrogenation Blocks

Next we investigate another doping pattern: block hydrogenation. The doping blocks are assumed to be of equal size squares distributed uniformly over the graphene sheet. The block doping pattern is then controlled by two parameters: coverage (area

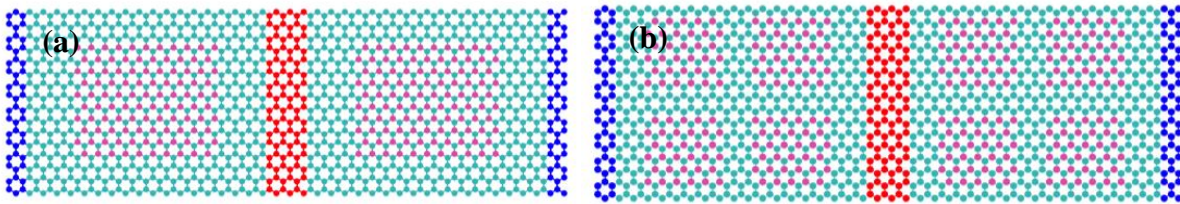


Figure 11: Schematic diagram of doping blocks on graphene

fraction of the doped regions) and size of the blocks. To study the effect of coverage and block size on the TC, a set of coverage values are chosen between 0% and 100%. For a given coverage, different number of doping blocks are used and TC is calculated for each of the doping pattern. For example, as shown in Fig. 11, for a given coverage, we can apply 2 doping blocks on the graphene as shown in Figure 11(a) or 8 blocks as shown in Figure 11 (b). With the same coverage, the block size is reduced in Figure 11 (b). In the NEMD simulations, periodic boundary condition is applied in the in-plane directions. The doping blocks start from center of the local section and separate with identical distance in both longitudinal and transverse directions.

Figure 12 shows the TC variation as a function of hydrogen coverage for two different sized blocks. The TC curves simultaneously show the effect of block coverage and block size. In all cases, TC decreases with increasing coverage in a non-linear manner,

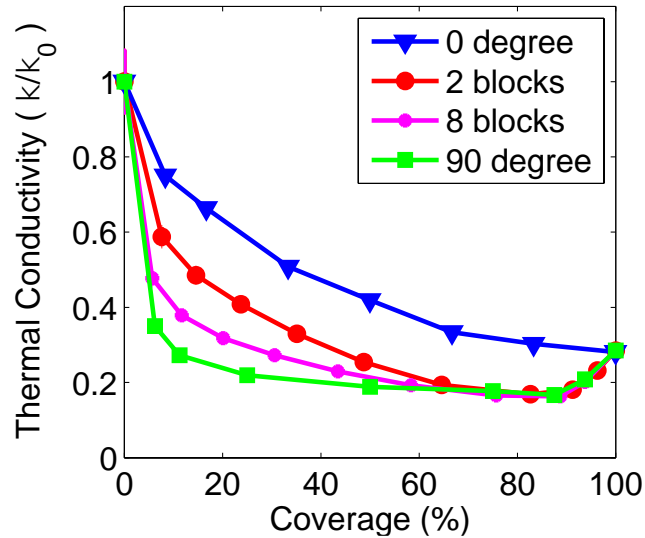


Figure 12: Graphene TC varies with coverage and number of blocks.

as shown in Fig. 12. Rate of decreasing is smaller at higher coverage region. The number of blocks and equivalently the size of the blocks, has a large influence on the TC at lower coverage region. With the same coverage, more, but smaller, blocks give a much smaller TC. As shown in Fig. 11, smaller blocks creates more interfaces between the doped and undoped regions. The average distance between the interfaces is also reduced. Therefore, more interface scattering and shorter phonon mean free path are introduced. As a result, the TC is smaller in comparison with that in graphene doped with large blocks. The effect of size and number of the blocks can be neglected at higher coverage, where interfaces begin to merge.

4.5 Thermal Conductivity Variation with Single-Side Hydrogenation Patterns

Since a graphene sheet with patterned single-side hydrogenation stripes can be relaxed to different deformation modes depending on both the size of H and its W/H ratio, it is important to understand how the deformation modes will affect the thermal conductivity. For a graphene sheet of the size $5.10 \text{ nm} \times 19.65 \text{ nm}$, we consider four different stripe lengths: $H = 4.91 \text{ nm}$, $H = 3.28 \text{ nm}$, $H = 2.46 \text{ nm}$ and $H = 1.97 \text{ nm}$, which are corresponding to the 2, 3, 4, and 5 stripes on each heat flux region, respectively. The hydrogenated graphene is then relaxed and the thermal conductivity is calculated. For comparison, we maintain the pre-stress along the heat flux direction due to the patterned hydrogenation and keep the planar form of the hydrogenated graphene, such that the deformation modes shown in Fig. 8(C–F) do not occur (NON mode). Thermal conductivity is then calculate for this unrelaxed configuration. Clearly, the difference in the thermal

conductivity of the relaxed and unrelaxed graphene sheets represents the effect of the global deformation modes on the thermal conductivity. Figure 13 shows the thermal conductivity of both relaxed and unrelaxed graphene sheets with varying H and W .

The thermal conductivity of relaxed and unrelaxed graphene sheet is represented by filled and empty circles, respectively. The size of the circles represents the magnitude of the thermal conductivity, as shown on the right side of Fig. 13. The color of filled circles represents the deformation mode. For unrelaxed graphene, the thermal conductivity decreases monotonically with increase of W or decrease of H . However, different trends are observed for the relaxed graphene sheet. The TRI deformation mode leads a higher decrement rate of the thermal conductivity. The COM deformation mode leads to a monotonically increasing trend of the thermal conductivity due to the closer packing of the carbon and hydrogen atoms as shown in Fig. 8. The graphene's thermal conductivity in the ROL modes monotonically increases with the hydrogen coverage. The thermal conductivity of aROL mode presents a relatively large fluctuation closely related with the unstable deformation mode.

To further understand the effect of deformation mode on the thermal conductivity variation, we compare the PDOS of unrelaxed and relaxed graphene sheets with various hydrogenation length W and a given stripe length $H = 4.91$ nm, shown in Fig. 14. The PDOS of the pristine graphene is plotted as green solid line for reference. The black solid lines represent the PDOS of unrelaxed graphene with different hydrogenation length W . The blue, cyan, and magenta dashed lines represent the TRI, COM and ROL deformation mode, respectively. In comparison of the relaxed and unrelaxed hydrogenated graphene,

while the thermal conductivity can be affected by the following two factors: the position and the amplitude of the G-band, the latter plays a more important role. In the TRI mode

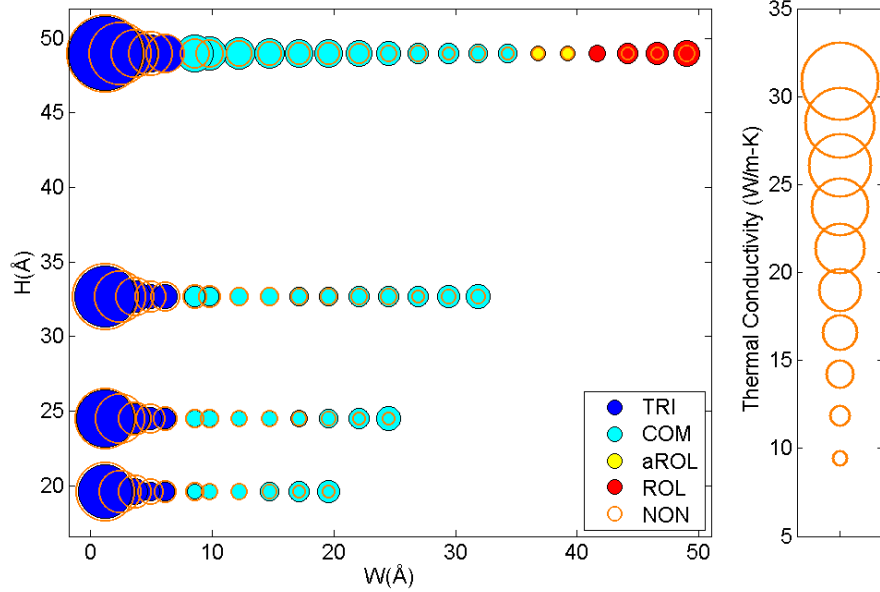


Figure 13: Thermal conductivity variation with hydrogenation length W and stripe length H . The graphene sheet has the size of $5.10 \text{ nm} \times 19.65 \text{ nm}$. The size of empty circles represents the magnitude of thermal conductivity of the unrelaxed graphene sheet with patterned hydrogenation. The size and color of the filled circles represent the magnitude of thermal conductivity and the deformation mode of the relaxed graphene sheet with patterned hydrogenation.

case ($W = 0.25 \text{ nm}$), the red-shift of the G-band for the unrelaxed graphene sheet is due to the external tensile stress applied to keep the graphene planar. Although the G-band for the relaxed graphene sheet (TRI mode) does not shift to the left, the amplitude decreases significantly. As discussed previously, the decreasing amplitude is related with the left shift of acoustic phonons, resulting in a lower thermal conductivity. For the COM case ($W = 1.97 \text{ nm}$) and the ROL case ($W = 4.67 \text{ nm}$), the position of the G-bands are similar for both the unrelaxed and relaxed graphene sheets. It shows that, for high doping density cases, the

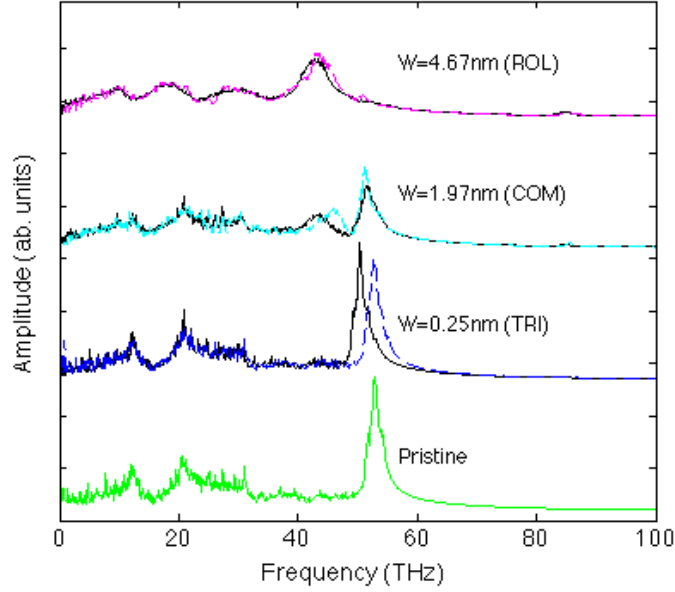


Figure 14: Comparison of PDOS between unrelaxed (solid line) and relaxed (dash line) graphene with various hydrogenation length W . The length of the stripe H is 4.91 nm.

hydrogen doping determines the PDOS and the effect of stretching on the G-band position becomes insignificant. However, the amplitude of the G-band is higher for the relaxed graphene sheets, which implies a higher thermal conductivity when they are in relaxed COM and ROL modes.

4.6 Summary

In summary, we investigate the thermal conductivity variation of graphene with respect to patterned hydrogenation, doping density and the deformation modes induced by hydrogenation through non-equilibrium molecular dynamics simulations. By relaxing the local stress in hydrogenated graphene sheets, various deformation modes are observed.

First principles theory calculations are performed to model and explain the relation between the bending slope of the graphene sheet and the length of the hydrogenation region. Our simulation results show that, when the W/H ratio increases, the thermal conductivity decreases quickly under the TRI mode and exhibits an increasing trend under the COM mode. This study illustrates a new opportunity to control both the thermal conductivity and the deformation mode of graphene through patterned hydrogenation. Meanwhile, it demonstrates that great attention is necessarily to be paid to the thermal conductivity variations in graphene based foldable devices.

CHAPTER 5 THERMAL CONDUCTIVITY VARIATION OF GRAPHENE WITH PATTERNED DOUBLE-SIDE HYDROGENATION

As discussed in Chapter 4, thermal conductivity of graphene can be significantly changed by hydrogenation coverage and deformation modes. It is demonstrated that TC of graphene significantly decreases with doping hydrogen atoms due to localized change in atomic bonds. Various doping patterns can also induce geometry change and thermal rectification in graphene. While patterned hydrogenation is being recognized as an effective way to modify or control the material properties of graphene for various applications, the fundamental physical mechanisms of graphene TC variation due to patterned hydrogen doping has not been well understood. In this study, we adopt non-equilibrium molecular dynamics (NEMD) method to investigate the thermal conductivity variation of graphene with different hydrogenation coverage and doping orientation. We consider double side hydrogen doping stripes in different orientations with the coverage from 0% to 100%. We calculate the effect of doping coverage and orientation on phonon density of states (PDOS), phonon dispersion relation, phonon relaxation time and the specific heat. Based on the kinetic theory of lattice thermal transport, the physical mechanisms of the thermal conductivity variation induced by patterned hydrogenation of graphene are revealed.

5.1 Simulation Setup

The open source code LAMMPS[90] is again adopted in this study to perform the non-equilibrium molecular dynamics simulation with the AIREBO potential describing the

interaction among carbon and hydrogen atoms.[92][64]. The torsional term in AIREBO is turned off as it leads to an underestimation of thermal conductivity. Since the chirality dependence of TC is negligible with the comparison of the length dependence, we adopt a graphene lattice of $19.6 \text{ nm} \times 5.1 \text{ nm}$ with the heat flux direction in zigzag direction as shown in Fig. 15(a). As before, the graphene is decomposed into the hot region, cold region and heat conduction regions. Periodic boundary condition is applied in the in-plane x - and y -directions while a 20 nm thick vacuum is maintained in z -direction to avoid out of plane interaction.

The time step is 0.5fs. Since MD is classical simulation with the temperature T_{MD} calculated from the kinetic energy of atoms based on the Boltzmann distribution. Quantum corrections need to be applied when the temperature is below the Debye temperature[99]. The commonly-used quantum correction approaches for thermal properties are based on temperature correction, where the Classical MD temperature can be corrected with the quantum correction as [100]

$$3Nk_B T_{MD} = \int D(\omega) n(\omega, T_{QC}) \hbar \omega d\omega \quad (5.1)$$

where T_{MD} is MD temperature, T_{QC} is the quantum corrected temperature, $D(\omega)$ is the phonon density of states. However the temperature correction described above is based on ad-hoc arguments rather than fundamental theory. To date, there is no consensus on whether or not to include the zero-point energy. It has been reported that such correction often does not lead to the correct results [99] [101]. Moreover, the reported Debye temperature of graphene[102]–[105] has been controversial and the thermal conductivity variation which does not directly depend on the accurate value of temperature, researchers

has reported that the effect of quantum correction is trivial to such study [106][107]. Also the concern of this work is mainly the thermal conductivity variation due to patterned hydrogen doping, which does not directly depend on the exact value of the “correct” temperature. Therefore, we will not consider the quantum correction in this work.

With the isothermal-isobaric ensemble (NPT), we firstly take 50ps for the initial graphene structure to reach the equilibrium state at 300 K and continue run another 300ps. The relaxed graphene shows a slightly wrinkle plane structure. Then with the micro-canonical ensemble (NVE), a heat flux is generated, with the conservation of the total energy, by exchanging the velocity of the lowest kinetic energy atom in the hot region with the velocity of the highest kinetic energy atom in the cold region [108]. After the steady state is achieved with 100ps, this non-equilibrium simulation is continued to run 400ps for the need of post-processing. The procedure of computing the TC is as described in Section 2.3.

5.2 Thermal Conductivity

With the objective of understanding the thermal conductivity variation with hydrogenation coverage and doping orientation, we systematically conduct a series of calculations for graphene with hydrogenation stripes in three different orientations, 0 degree, 30 degree and 90 degree, shown in Figure 15(b, c, d), respectively. Hydrogen atoms are doped onto both sides of graphene alternatively as shown in Figure 15(d). The carbon bonds with hydrogenation change from sp^2 to sp^3 , resulting in different thermal properties.

With the coverage defined as the ratio of total number of hydrogen atoms over total number

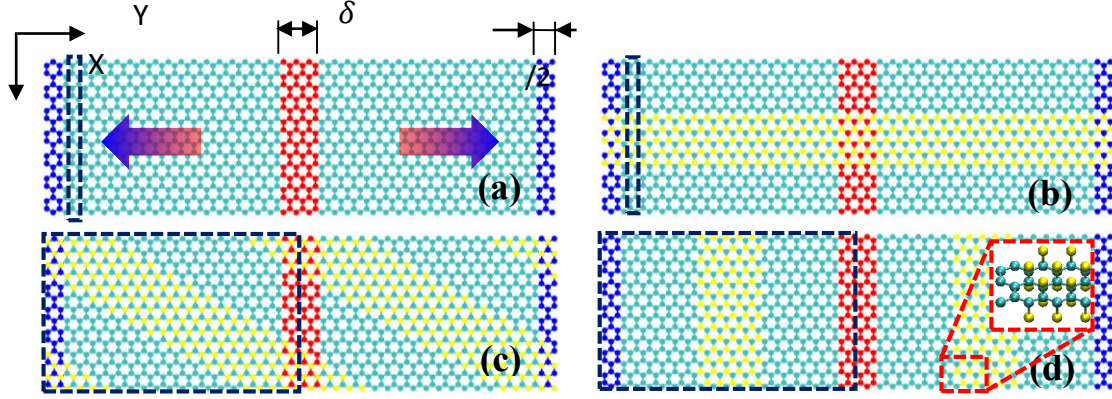


Figure 15: Schematic NEMD model of graphene with the heat source region (red, δ is the width of the region), heat sink regions (blue), and heat flux regions (cyan). (a) pristine graphene; (b) longitudinal hydrogen doping stripes (0 degree); (c) 30 degree angular hydrogen doping stripes; and (d) transverse hydrogen doping stripes (90 degree). The subplot in (d) represents the graphene lattice with hydrogen doping (C: cyan, H: yellow). All the black dash boxes represent the unit cell for SED calculation, respectively.

of carbon atoms within the system, we calculate the thermal conductivity with the hydrogenation coverage from 0% (pristine graphene) to 100% (graphane) and normalize it by the value of pristine graphene. For the pristine graphene shown in Figure 15(a), we calculate the thermal conductivity as $\kappa_0=74.3\text{W/m-K}$, which is in good agreement with previous results [22]. The relaxed graphene with stripe doping shows obvious wrinkle structure than the rippling of perfect graphene, especially the 30° angle doping. However, we prove that the thermal conductivity difference due to the morphology effect can be neglected. Coverage and orientation are the dominating factors in determining thermal conductivity variation.

As shown in

, thermal conductivity presents a decreasing trend with increasing coverage, regardless of doping stripe orientation. For 0 degree doping case, TC decreases gradually through the doping coverage. For the 90 degree doping stripe case, TC has a sharp decline at lower doping coverage (less than 20%), proceeds with a slow decline rate till the coverage approaching 90% and presents a slight increase after that. It is because the thermal conductivity is mainly determined by the interface that is perpendicular to heat flux direction. Once the interface is created, even at low coverage, all phonon transport in heat flux direction will be scattered significantly. When the doping coverage is between 20% and 90%, the interfacial scattering maintains dominate to determine the thermal conductivity, therefore the gradient of thermal conductivity variation is very small. As the doping coverage approaching 100%, the interfaces overlap with each other and diminish, causing an increment of TC. For the 30 degree oriented doping stripe case, the behavior of TC variation with doping coverage lies in between the 0 degree case and 90 degree case.

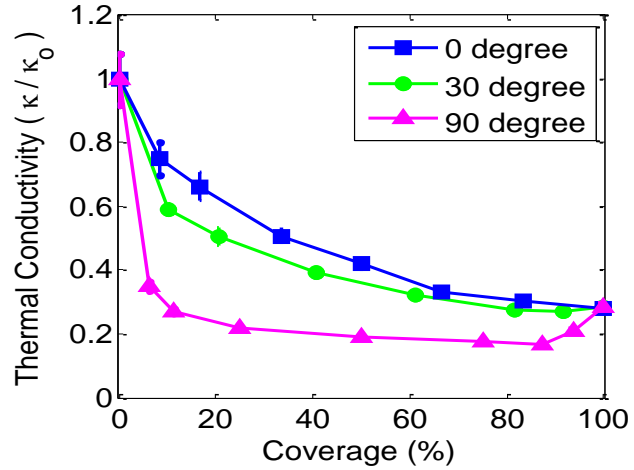


Figure 16: Thermal conductivity of graphene with longitudinal (0 degree), transverse (90 degree) and 30 degree angular doping stripes.

In order to thoroughly understand the relation between

thermal conductivity variation with the doping coverage and doping stripe orientation, we

recall the thermal conductivity definition based on the kinetic theory of the lattice thermal transport, Eq. (2.23) which indicates the direct factors of the thermal conductivity: phonon group velocity, relaxation time and specific heat of the phonon branches. Therefore, we integrate the spectrum energy density (SED) method[109] with our MD simulation to evaluate the anharmonic phonon properties of carbon atoms in the hydrogen doping graphene [110], including the relaxation time and phonon group velocity. Furthermore, by using the Fourier transform of the velocity autocorrelation, the PDOS and specific heat can be evaluated.

5.3 Phonon Dispersion

The phonon dispersion curves are useful in determining several physical quantities such as phonon group velocities of different phonon branches and elastic modulus of the material. For crystalline materials, the phonon dispersion curves can be obtained from the spectral energy density (SED) function $\Phi(\mathbf{k}, \omega)$. In order to calculate phonon SED, we first define the SED unit cell as the smallest group of atoms repeating along the heat flux direction, highlighted with the black dash rectangle boxes in Figure 15. For 0 degree doped graphene, the SED unit cell contains 48 atoms within two layers of carbon atoms along the heat flux direction. We define this unit cell as small SED unit cell with the lattice constant $a_s = \sqrt{3}a_{C-C}$. For 30 degree and 90 degree doped graphene, we take the entire supercell as SED unit cell to calculate phonon dispersion, based on which we estimate phonon group velocity and phonon relaxation time. To our knowledge, similar studies have been done for other material systems. For example, Larkin [111] studied argon-silicon alloy system with

disorder supercell and predicted phonon properties including PDOS, phonon relaxation time. Hori et al. [112] treated the entire supercell of silicon-germanium alloy as the primitive unit cell to calculate the dispersion relation. In our work, the SED unit cell contains 1920 atoms in between the cold region and hot region due to the symmetry. We define this unit cell as large SED unit cell with the lattice constant $a_L = 40\sqrt{3}a_{c-c}$. With respect to different doping cases, we adopt 90 small unit cells and 50 large unit cells along the heat flux direction, respectively, and perform the equilibrium MD simulations at 300K with time step 0.2fs for 100ps. With the NEMD simulation of the doped graphene system, the phonon SED can be computed by using Eq. (2.25). The method to calculate $\Phi(\mathbf{k}, \omega)$ using the velocity history of the atoms obtained from NEMD simulation is described in Chapter 2. Plotting $\Phi(\mathbf{k}, \omega)$ in a 2-D figure with \mathbf{k} as the x-axis, $f = \omega/2\pi$ as the y-axis and a color code representing the magnitude of $\Phi(\mathbf{k}, \omega)$, we obtain the phonon dispersion curves along the direction of wave vector \mathbf{k} . The wave vector \mathbf{k} is in direction from Γ point to K point, which is corresponding to zigzag graphene direction in real space. The resolution of wave vector \mathbf{k} is based on the number of SED unit cell along the heat flux direction. Here it is discretized into $N_l/2$ points ranging from 0 to π/a with a as the lattice constant.

Figure 17 represents the phonon dispersion relation of 0 degree doping stripe case (top) and 90 degree doping stripe case (bottom) with the doping coverage of 0%, 25%, 50%, 75% and 100%, respectively. Dispersion relation calculated from small SED unit cell follows a clear curve that starts from $k^* = 0$ and ends at $k^* = 1$, as shown in the top figure in Figure 17. The large SED unit cell of 90 degree doped graphene causes the many times

of dispersion curves folding such that the curves appear to be parallel. A down shift of dispersion curves can be clearly observed. Taking 0 degree case for example, the longitudinal acoustic (LA) phonon branch originates from 0 THz and ends at ~35 THz with pristine graphene (0% hydrogenation coverage), but shifts down to 20 THz with graphane (100% hydrogenation coverage). Similar downshift can also be observed with optical phonon branches. The maximum prime optical phonon frequency at Γ point ($k=0$) is 53 THz with 0% hydrogenation coverage, and decreases to 38 THz with 100% hydrogenation coverage. Since phonon group velocity is defined as $v = d\omega/d\mathbf{k}$, the large downshift of dispersion curves causes a significant reduction of phonon group velocity. The down shift of the dispersion curves and reduction in the group velocity can be, at least partially, explained from the force constant point of view. From the lattice dynamics theory, phonon dispersion can be evaluated by solving an eigenvalue problem of the force constant matrix. From our calculated strain-stress relation of pristine and doped graphene, it is found that hydrogen doping induces softening in the graphene lattice, causing lower acoustic group velocities.

As shown in Fig. 17, a new band of phonon modes (30 to 40 THz) with low phonon group velocities are presented when introducing hydrogenation onto graphene. These are optical phonon modes that scatter with other phonon modes, which caused a re-distribution of phonons. The original optical modes above the new band all fade out gradually as doping coverage increases. The acoustic branches below the new band become less concentrated, i.e., the originally sharp acoustic phonon dispersion curves become smeared. This result implies that the acoustic phonons, which contribute more to TC, are scattered more

significantly when the doping coverage increases. The blurry phonon dispersion curves manifest this important physical mechanism that contribute to the reduction of TC. In addition, comparing the top and bottom figures in Fig. 17, the acoustic branches with 0 degree doping stripe case are sharper than those with 90 degree doping stripe case. It shows that the acoustic phonons are less scattered in graphene with 0 degree doping stripes. This result implies a lower TC in the graphene with 90 degree doping stripes, which is observed in Figure 16.

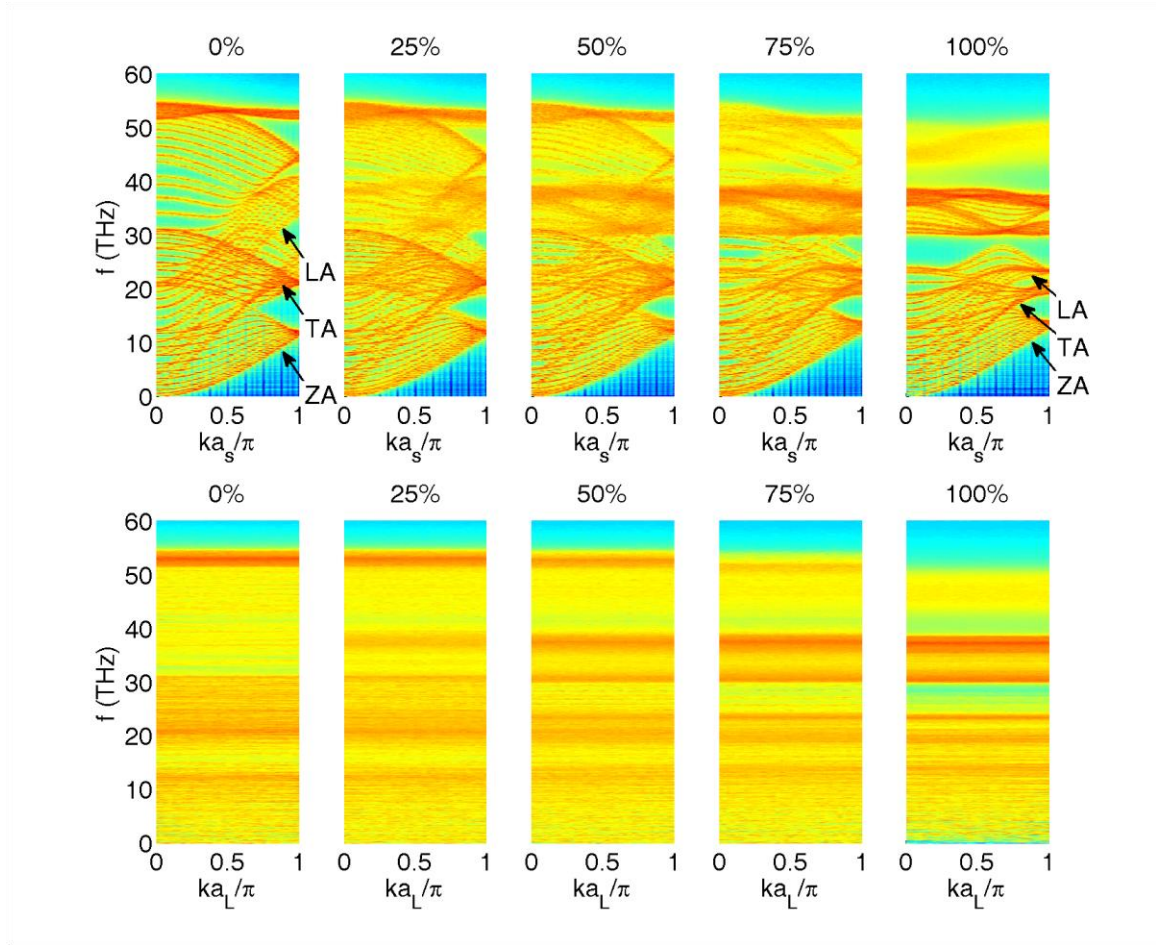


Figure 17: Dispersion relation of zigzag graphene with doping stripe angle of 0 degree (top) and 90 degree (bottom), $a_s = \sqrt{3}a_{C-C}$ and $a_L = 40\sqrt{3}a_{C-C}$ are lattice constants of small and large unit cell.

5.4 Phonon Relaxation Time

While the strength of phonon-phonon scattering is qualitatively depicted through the blurriness of the phonon dispersion curves shown in Fig. 17, it can be further quantified by calculating the phonon relaxation times. The SED function (Eq. 2.25) can be written as the sum of Lorentzian functions of all phonon branches as shown in Eq. (2.29).[76][113] Therefore, by fitting the spectral energy density obtained from Eq. (2.25) to the Lorentzian function form given in Eq. (2.29), the relaxation time of phonons, τ , can be evaluated. As shown in Fig. 17(a), the dispersion relation of pristine graphene is plotted by the phonon

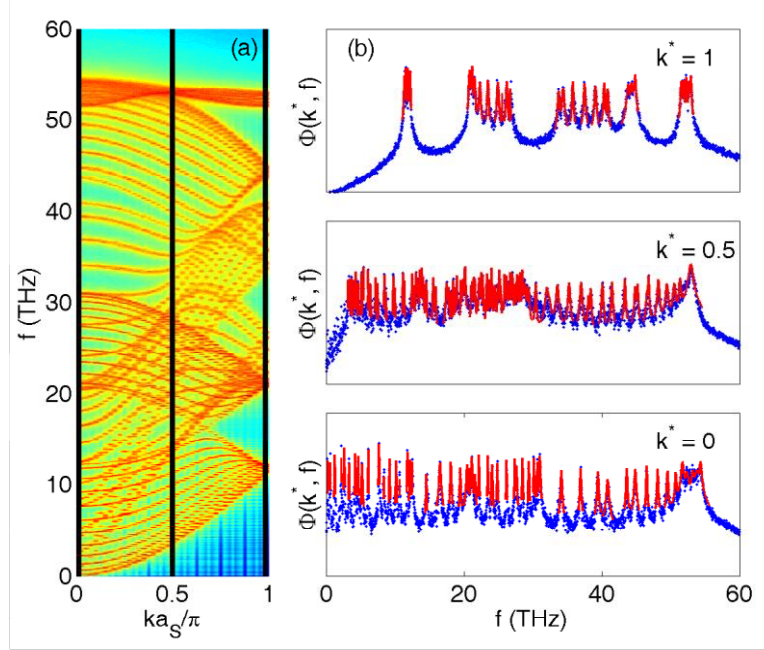


Figure 18: (a) Dispersion relation of pristine graphene; (b) spectral energy density of pristine graphene with $k^* = 0, 0.5$, and 1 ($k^* = ka_s/\pi$), $a_s = \sqrt{3}a_{C-C}$. Blue dots are the phonon SED, red lines are fitted to SED peaks to extract phonon relaxation time τ .

SED as the function of \mathbf{k} and ω . In Fig. 17(b), the phonon SED profiles at 3 selected wave

vectors are plotted as blue dots. Each peak represents a phonon branch or the degeneracy of several branches. By using the Levenberg-Marquarde algorithm, all peaks (shown as red line) can be fitted by multiple Lorentzian functions with the magnitude and frequency of peaks given from Figure 18(a) through the software Fityk [114]. Following this procedure,

the relaxation time, $\tau(\mathbf{k}, \nu)$ for all branches can be obtained. Figure 18 shows the comparison of relaxation times of graphene with 0 and 90 degree doping stripes. It is shown in Fig. 18 (a) that most of the acoustic phonons have higher relaxation time than those of optical phonons. When hydrogen atoms are fully doped onto graphene, as shown in Fig.

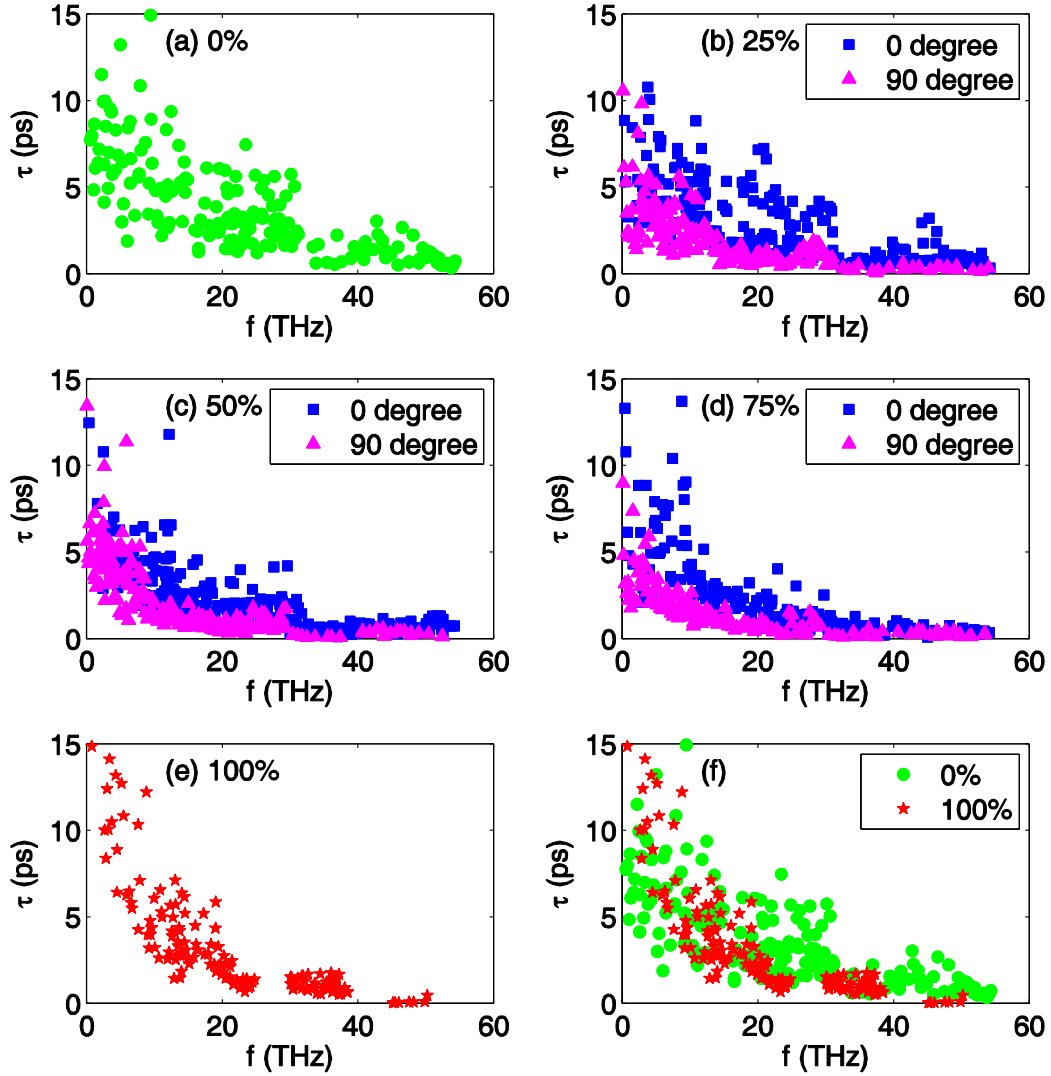


Figure 19: Frequency dependent relaxation time of graphene with hydrogen doping stripes, with doping coverage ranging from 0% to 100%. (b)-(d) also show relaxation time comparisons between 0 and 90 degree doping stripe orientations. (f) represents the comparison between 0% doping and 100% doping case.

18 (f), magnitudes of τ are reduced and the range of frequency largely shrinks, leading to a decrease of TC. The difference of TC for different doping stripe orientations with same doping coverage are presented in Fig. 18 (b), (c), and (d). The blue squares are for the 0 degree doping stripe case and the magenta triangles are for the 90 degree doping stripe case. It is clear that the relaxation times of 0 degree doping stripe case are larger than those with 90 degree doping stripe case. The effect of doping orientation on TC can clearly be attributed to the difference in the relaxation time.

5.5 Phonon Density of States and Specific Heat

Next we investigate the phonon density of states which is another important factor shown in Eq. (2.23). The PDOS is obtained by computing the Fourier transform of the velocity autocorrelation as shown in Eq. (2.22). Note that, the PDOS can also be obtained from the phonon SED method. The PDOS produced by the SED method and Eq. (2.22) are identical. However, the latter method is computational less expensive. Figure 19 illustrates the PDOS variation with doping coverage and stripe orientation.

As shown in Figure 20, with the increase of doping coverage, a red-shift of the G-band is observed, independent of the doping orientation. The red-shift of G-band represents a lowering of the LA phonon dispersion curve and a reduction of phonon velocity, which is consistent with the results shown in Figure 17. With the unit of joule per mole kelvin, the specific heat, C_V , can be calculated based on the PDOS as shown in Eq.

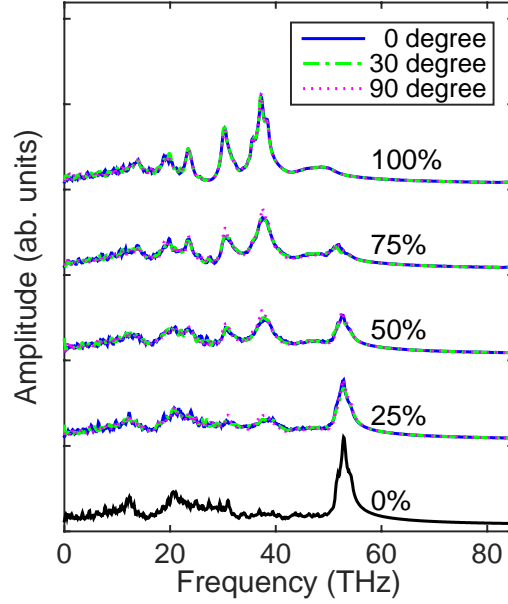


Figure 20: Phonon density of states variation with selective doping coverage and orientation

(2.24). Below the Debye temperature of graphene (~ 2100 K[115]), specific heat follows the Debye model and increases with temperature rather than hydrogenation. The fully doped graphene has a similar specific heat as that of pristine graphene at 300K.[89][116] As shown in Figure 21, both pristine graphene (coverage = 0%) and doped graphene (coverage = 50%) have a similar specific heat, which increases with temperature and tends to converge, at high temperature, to 24.94 J/mol-K, the classical limit defined by Dulong-Petit law [89]. The convergence of specific heat at high temperature is due to the fact that

$Y(\omega, T) = \left(\frac{\hbar\omega}{k_B T}\right)^2 e^{\frac{\hbar\omega}{k_B T}} / \left(e^{\frac{\hbar\omega}{k_B T}} - 1\right)^2$ in Eq. (2.24) represents a probability distribution enlarging with temperature increase. When temperature is lower, $Y(\omega, T)$ is much larger

for low frequencies than for high frequencies, meaning the specific heat is mainly contributed by low frequency phonons. It is shown in Fig. 20 that the pristine and doped graphene have similar PDOS in the low frequency range. Therefore, their specific heat at lower temperatures are similar. For this reason, the specific heat variation due to the hydrogenation is small and C_V does not play a role in the hydrogenation induced TC reduction.

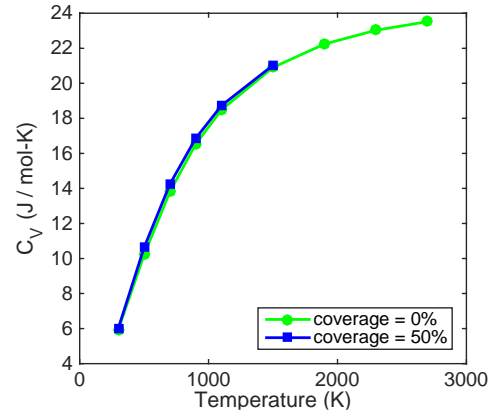


Figure 21: Temperature dependence of specific heat of pristine and longitudinally doped graphene.

In summary, the TC variation with doping coverage shown in Figure 16 can be attributed to the combined action of phonon group velocity reduction and phonon-phonon scattering relaxation time reduction. The difference between the TC curves for different doping stripe orientations is mainly due to the difference in relaxation time. The 0 degree stripes construct such a doping pattern that reduces the coverage of sp^2 C-C bonding without interrupting the thermal transport in the heat flux direction. As the doping coverage increases, the TC is reduced gradually due to the continuous decrease in acoustic phonon group velocity and phonon relaxation time. In contrast, the 90 degree doping stripes introduce thermal barriers perpendicular to the heat flux direction, blocking the heat flux most significantly, and thus abruptly reducing the phonon relaxation time as shown in Fig. 19 (b) even with a small coverage of hydrogen atoms. When the coverage is higher than 85%, the neighboring thermal interface regions created by the 90 degree doping stripes

begin to overlap and diminish at 100% coverage, leading to a small increase of mean free path and TC. The effect of 30 degree doping stripes can be understood as a transition state between the 0 and 90 degree doping effects.

5.6 Summary

In this chapter, we adopt non-equilibrium molecular dynamics to study the thermal conductivity variation of graphene with patterned hydrogen doping with respect to doping coverage and doping stripe orientation. Our simulation results show that TC of hydrogenated graphene have different decreasing trends with different doping stripe orientation. The phonon dispersion curves of the hydrogenated graphene reveals that the doping causes a reduction in phonon group velocity and an increase in phonon-phonon scattering. The phonon relaxation time, obtained by fitting Lorentzian function to the phonon SED profile, exhibits the distinct effect of doping stripe orientations. Larger angle between the doping stripe orientation and the heat flux direction leads to smaller relaxation times, i.e., stronger phonon-phonon scattering. Finally, it is found that the specific heat does not play a role in the hydrogenation induced TC reduction.

CHAPTER 6 THERMAL RECTIFICATION IN GRAPHENE WITH TRIANGLE DOPING PATTERN

We have studied strain effect, chirality effect, temperature effect on thermal transport in graphene. We have also explored tuning the thermal conductivity through hydrogenation. The possibility of widely tuning thermal conductivity by using strain, temperature, and chemical functionalization extends the design space of graphene based devices. Beyond these design parameters, thermal rectification is another important behavior and design target for thermal management and control of nano-devices. Thermal rectification phenomenon represents the thermal transport dependence of temperature gradient along a specific axis. As desirable thermal rectifying materials in thermal management application, they can exhibit high thermal conductivity in one direction for efficient thermal transport and low thermal conductivity in the opposite direction for temperature insulation and protection of heat flux sensitive components. Similar to the electronic diodes in electronic circuit, thermal rectifiers are the essential components in designing advanced thermal management systems such as thermal diodes, thermal transistors and thermal logic circuits. It is necessary to design two-dimensional thermal switches in order to cool electronics effectively in the future as device sizes become smaller with a stacked chip design trend and more complicated thermal management problems [117]. Researchers has present the high thermal rectification of triangular shape graphene nano-ribbons and cone shape carbon nanotube both from experiments and from calculation[43], [48], [50], [51], [53], [106], [118], [119]. However, the mechanisms behind such thermal rectification behavior is lack of thoroughly understanding. In this

chapter, we first study thermal rectification in hydrogenated graphene sheet with asymmetric triangular doping patterns. Then we elucidate the effects of mass and bonding strength to the thermal rectification behavior in order to fully understand the design space and parameters in the future thermal rectifier design and development.

6.1 Molecular Dynamics Setup

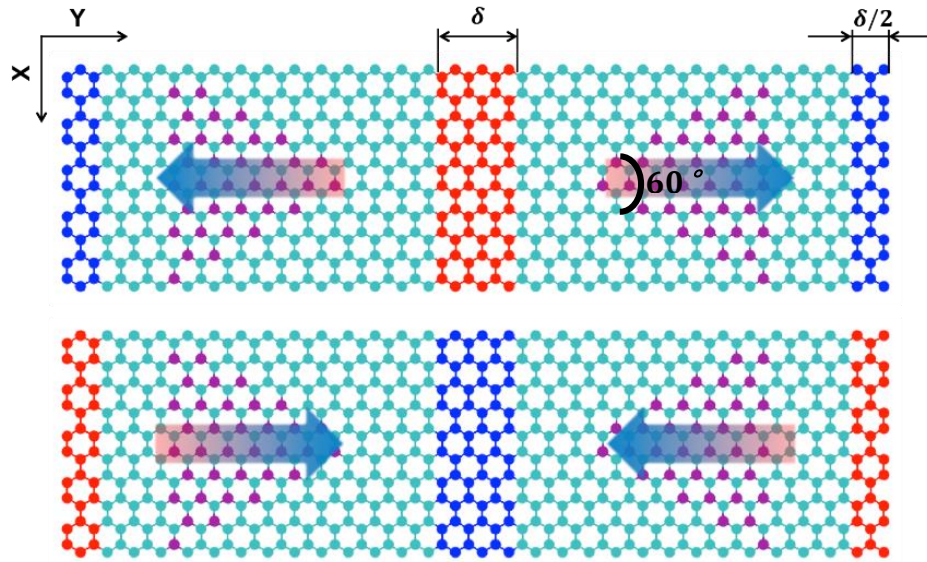


Figure 22: Schematic model of graphene with triangle doping pattern.

To study the thermal rectification in hydrogenated graphene, we dope the graphene sheet of $19.6nm \times 5nm$ with hydrogen with 60 degree triangular patterns as shown in Fig. 22. We perform two NEMD simulations with opposite heat fluxes along the zigzag direction, respectively. The heat flux direction from the center to the edges is denoted as J_+ (top figure) and the heat flux direction from the edges to the center is denoted as J_- .

The thermal conductivities κ_+ and κ_- are calculated respectively. Therefore, thermal rectification (TR) can be defined as,

$$TR = \frac{\kappa_+ - \kappa_-}{\kappa_-} \times 100\% \quad (6.1)$$

6.2 Thermal Rectification of Triangular Hydrogenated Graphene under Strain Effect

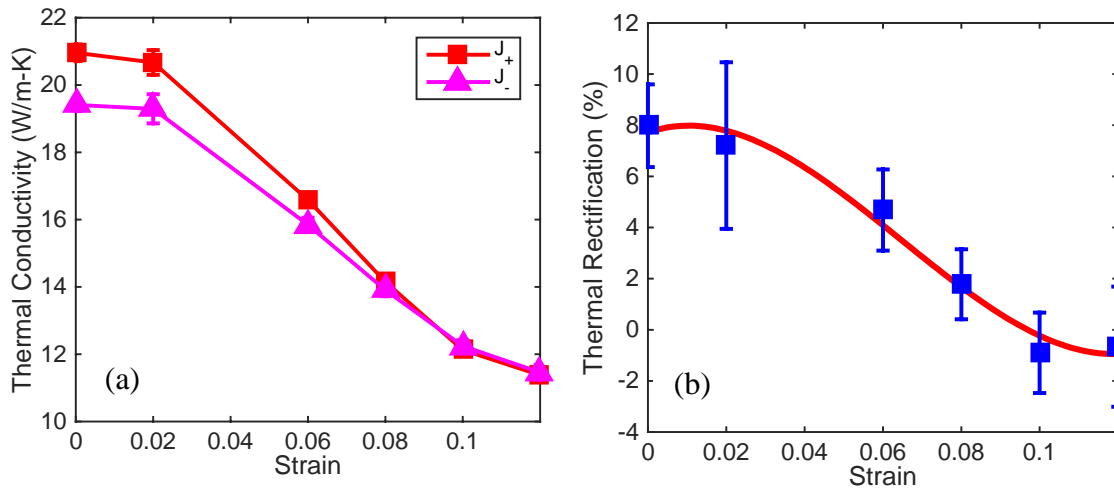


Figure 23 Thermal conductivity (a) and thermal rectification (b) of triangular doped graphene in Fig. 22.

Figure 23(a) shows the thermal conductivity as a function of strain in triangular doped graphene with heat fluxes in two opposite directions. In both cases, the TC declines gradually with tensile strain increases from 0 to 0.12. Since all conditions are the same except for heat flux direction, the difference in TC is clearly originated from the asymmetry of triangular doping pattern. Thermal resistance due to the doping increases gradually as heat flux flows from center to the edge while it decreases gradually as heat flux flows in the reverse direction. This difference becomes smaller as the tensile strain increases and

negligible when the strain is approaching 8%. The large strain effect dominates the decrease of thermal conductivity. The thermal rectification curve shown in Figure 23 (b) indicates that the highest value occurs when no strain is applied. TR becomes less significant with larger strain. There are two factors cause the asymmetry of system. Doping pattern introduces asymmetry of geometry and tensile strain adds a force constant difference in doping and pristine region. As mentioned in Wu [48], asymmetry of force constant distribution can either enhance or compensate the effect of other asymmetry condition on thermal rectification. In our study, it is clear that the asymmetry of force

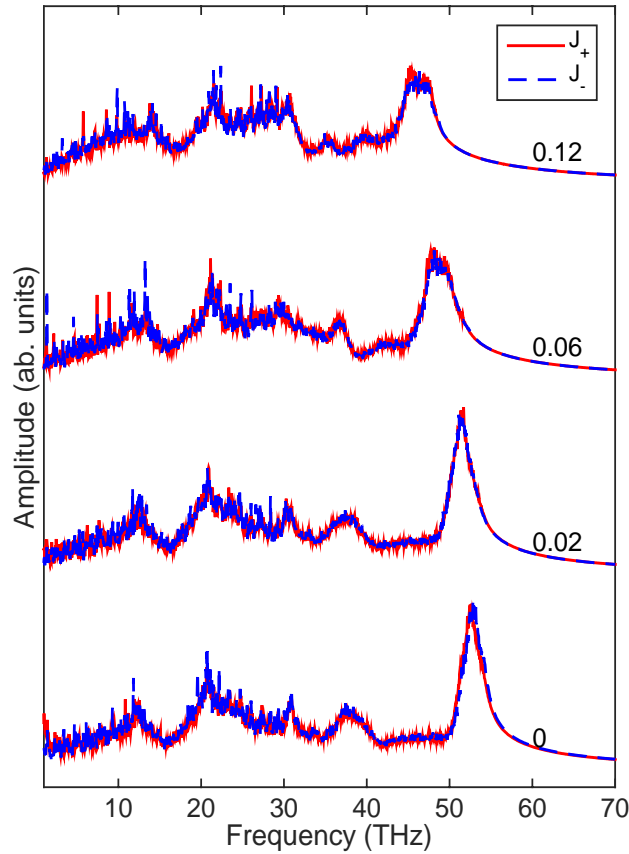


Figure 24 Total PDOS of triangular doped graphene with J_+ and J_- .

constant induced by strain in graphene with triangle doping pattern will counteract the effect of doping pattern on thermal rectification.

In order to understand the mechanism responsible for this phenomena, we calculate phonon density of states in triangular doped graphene with both J_+ and J_- as shown in Figure 24. The numbers sitting on each PDOS curve represents tensile strain. It is shown that red-shift of G-band caused by the strain are the same for both J_+ and J_- , corresponding to the reduction of thermal conductivity. However, we can hardly explain the difference of TC caused by asymmetric doping pattern at the same strain since PDOS of J_+ and J_- overlaps each other for all frequency. Therefore, this PDOS can only reflect the effect of external strain but not the effect of asymmetry of doping pattern.

6.3 Thermal Rectification Controlling Parameters

Since it is not practical to explain thermal rectification effect from the total PDOS as we discussed before, we plan to systemically investigate all the design parameters in the model shown in Figure 22 to understand their contribution to the thermal rectification, such as the shape of doped area, the system size, the mass of the doped area and the bonding strength between matrix atom and doped atom within the system. Therefore, we would thoroughly understand which parameters play dominate role in the design of large thermal rectification.

6.3.1 Asymmetric Doping Shape Effect

The thermal rectification is mainly depending on the asymmetric system shape or the asymmetric doped region along the heat flux direction. In Figure 22, the angle pointing to the heat flux direction is defined as $\Theta=60^\circ$. It can be used to define the length of carbon-

hydrogen interface ($W/\sin(\Theta/2)$). As two extreme cases when $\Theta=0^\circ$ or 180° , no thermal rectification effects exist. It is because no geometry asymmetry exists between the heat transfer direction from hot region to cold region and the heat transfer direction from cold region to hot region. Therefore, an optimized value must exist in order to reach the highest thermal rectification. To prove this hypothesis, we also investigated the thermal conductivity and thermal rectification of triangular hydrogenated graphene with a small angle (30°), as presented in Figure 25. Compared with the results from the model in Figure 22, thermal rectification decreases slightly and the strain effect thermal rectification variation is also limited.

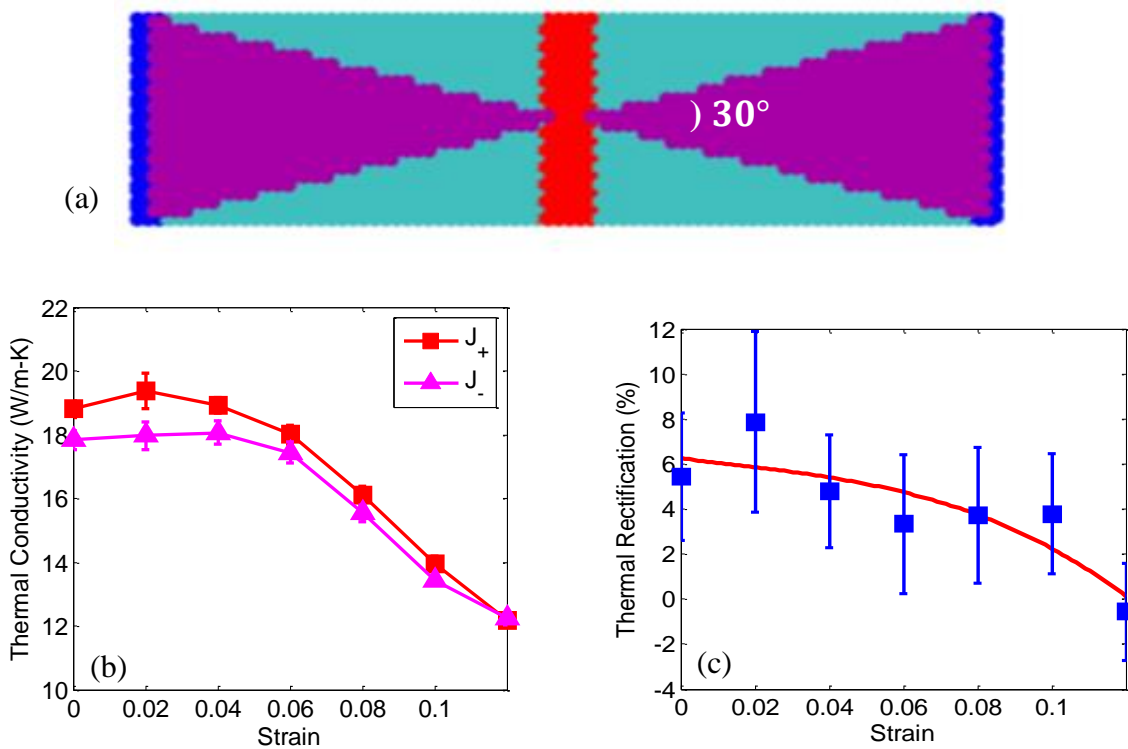


Figure 25 Thermal conductivity (b) and thermal rectification (c) of 30 degree triangular doped graphene (a).

6.3.2 Asymmetric Doping Size Effect

The model in the Fig. 22 is 5nm in width and 19.6nm in length. The length of equilateral hydrogenated triangle is 4.3nm. Due to the limitation of the simulation box size, phonons with longer wavelength than 19.6nm cannot be captured. The boundary scattering of phonons dominates in this ballistic regime. Therefore the thermal conductivity is underestimated comparing with the actual value. In order to investigate the asymmetric doping size effect, we increase the length of equilateral hydrogenated triangle to be 8.6 nm, two times of the previous model (Figure 22). In order to keep the matrix/doping ratio, we increase the simulation domain size to be 10nm in width and 39.2nm in length. The thermal conductivity increases since more phonons can be captured and boundary scattering of the nanomaterials becomes less significant, shown in Figure 26(a). However, the difference between thermal conductivity in J_+ and J_- direction remain unchanged. As we can see in Figure 26 (b), the thermal rectification is around 75% lower compared with the previous

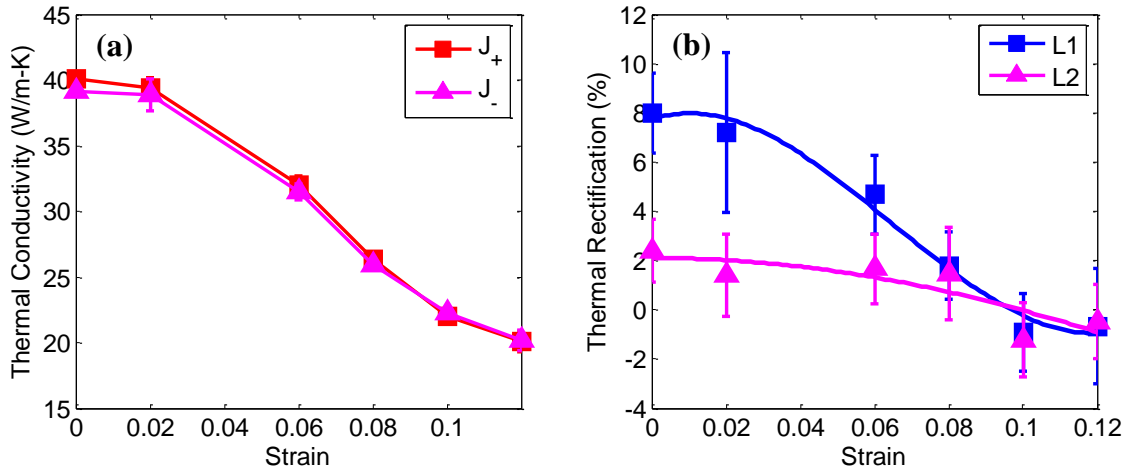


Figure 26 Thermal conductivity (a) of 60 degree triangular doped graphene with and comparison of thermal rectification (b) of triangular doped graphene with 5×19.6 nm (L1) and that with 10×39.3 nm (L2).

value (Fig.23). It shows that the thermal rectification is mainly depending on the phonon-phonon scattering along the matrix-doping interface. The more significant the phonon-phonon scattering, the stronger the thermal rectification.

We considered the doping shape effect and doping size effect based on the hydrogen doping, which the mass ratio of dopant/matrix is 1/12 (H/C). At the same time, the hydrogen-carbon bonding is relative weak comparing to the carbon-carbon bonding. In the next two sections, we will artificially manipulate the mass ratio of dopant /matrix and the bonding strength between the doping atom and matrix atom based on the availability of empirical potential in the MD simulation. The objective is to understand how mass ratio and bonding strength affect the thermal rectification factor of the system.

6.3.3 Mass Effect

Atomic mass plays an important role in thermal rectification by inducing asymmetry of vibration modes due to mass gradient in the heat flux direction. In this section, we change atomic mass of atoms in the triangle pattern while keeping matrix atom (carbon) unchanged elsewhere as shown in Figure 27. In this way, we artificially create a graphene with triangle dopant of various atomic masses. A mass gradient in heat flux direction is established. We adopt AIREBO potential without torsion term for all the interactions among carbon atoms and atoms with various atomic mass. The atomic mass ratio is defined as the ratio of atom mass in triangle pattern to the atom mass of carbon in the matrix. With NEMD simulations, we generate heat flux J_+ from center to edge and J_- in the reverse direction. The temperature profiles of various mass ratio are shown in Figure 27. With same amount of heat flux induced into the system, the temperature profiles look different.

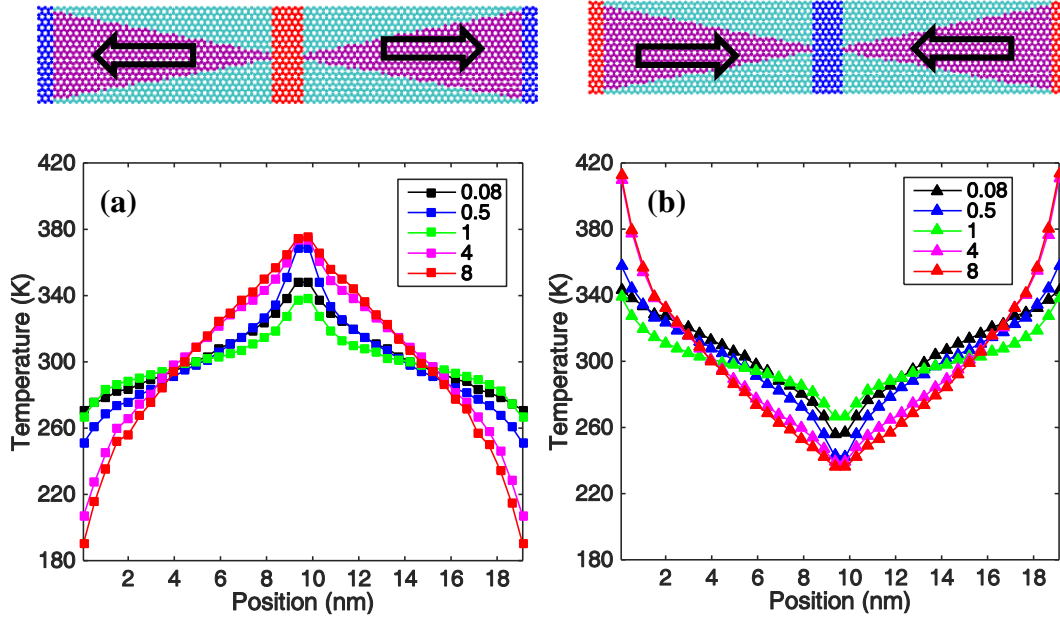


Figure 27 Mass effect on temperature profile with different heat flux direction. (a): J_+ heat flux direction is from the center to the edge; (b) J_- heat flux direction is from the edge to the center. Legend shows atomic mass ratio changes from 0.08 to 8.

With the increasing of the mass ratio which is larger than 1, the temperature difference at the hot region and cold region of the system increases. Therefore, the thermal conductivity decreases with the increasing of the mass ratio (>1), shown in Figure 28 (a). Temperature difference at the hot region and cold region of the system also increases with decreasing mass ratio, indicating lower thermal conductivity as shown in Figure 28(a).

In Figure 28 (a), a peak is reached at atomic mass ratio equals to 1, which demonstrates highest thermal conductivity of pristine graphene with uniform mass. Thermal conductivity drops significantly when the atomic mass ratio is away from unit. This indicates that mass gradient has negative effect on thermal transport since various atom masses will lead to different phonon vibration modes.

Figure 28(b) shows that thermal rectification changes with atomic mass ratio. Thermal rectification closes to 0 when ratio equals to 1 while it deviates from 0 when ratio is different. It indicates that there is no thermal rectification for pristine graphene with uniform mass. Thermal rectification can be introduced by mass difference in the heat flux direction. Interestingly, we observe a positive thermal rectification with atomic mass ratio < 1 and negative thermal rectification with atomic mass ratio > 1 . A positive thermal rectification represents that thermal conductivity in heat flux J_+ is larger than thermal conductivity in J_- direction and vice versa. When ratio < 1 , the J_+ is the direction of decreasing mass. When ratio > 1 , J_- is direction of decreasing mass. Therefore, we reach to the conclusion that heat conduction prefers the mass decreases direction.

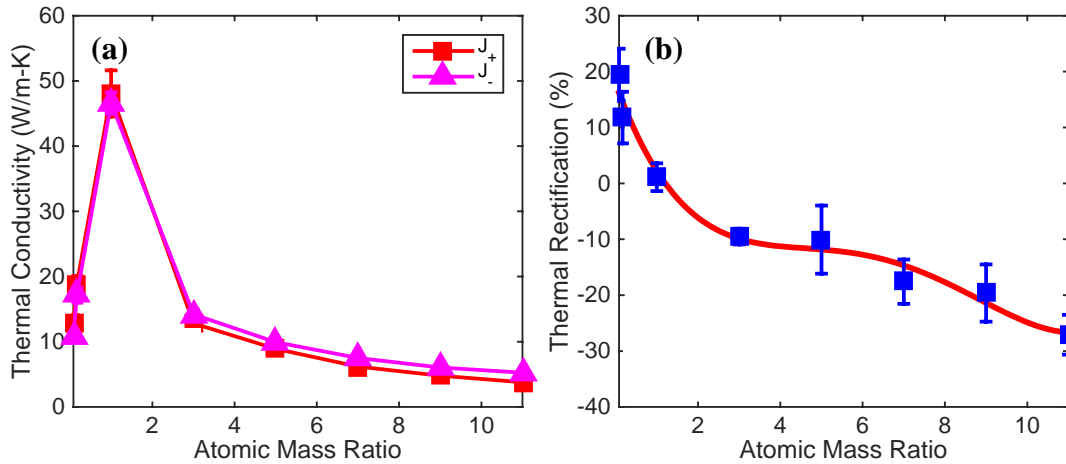


Figure 28 Thermal conductivity (a) and thermal rectification (b) of triangle patterned graphene of various masses.

Figure 29 shows the local PDOS of doped graphene on the Left Side and Center Region with different heat flux directions and various mass ratios. The Left Side is dominated by dopants, while the Center Region is dominated by carbon atoms. It is shown that the PDOS shifts from high frequency to low frequency with increasing atomic mass

on the Left Side, while the PDOS remains similar shape except the appearance of higher frequencies phonons with the mass ratio less than 1 on the Center Region. It indicates that lighter atoms in the triangle pattern introduce more high frequency phonons into the system. In order to understand the heat transfer mechanism, we need to consider the difference of PDOS transmission from one location to another. With mass ratio < 1 in J_+ direction, PDOS transmits with more low frequency phonons in the Center Region to a wide range of frequency phonons in the Left Side. With mass ratio < 1 in J_- direction, PDOS transmits

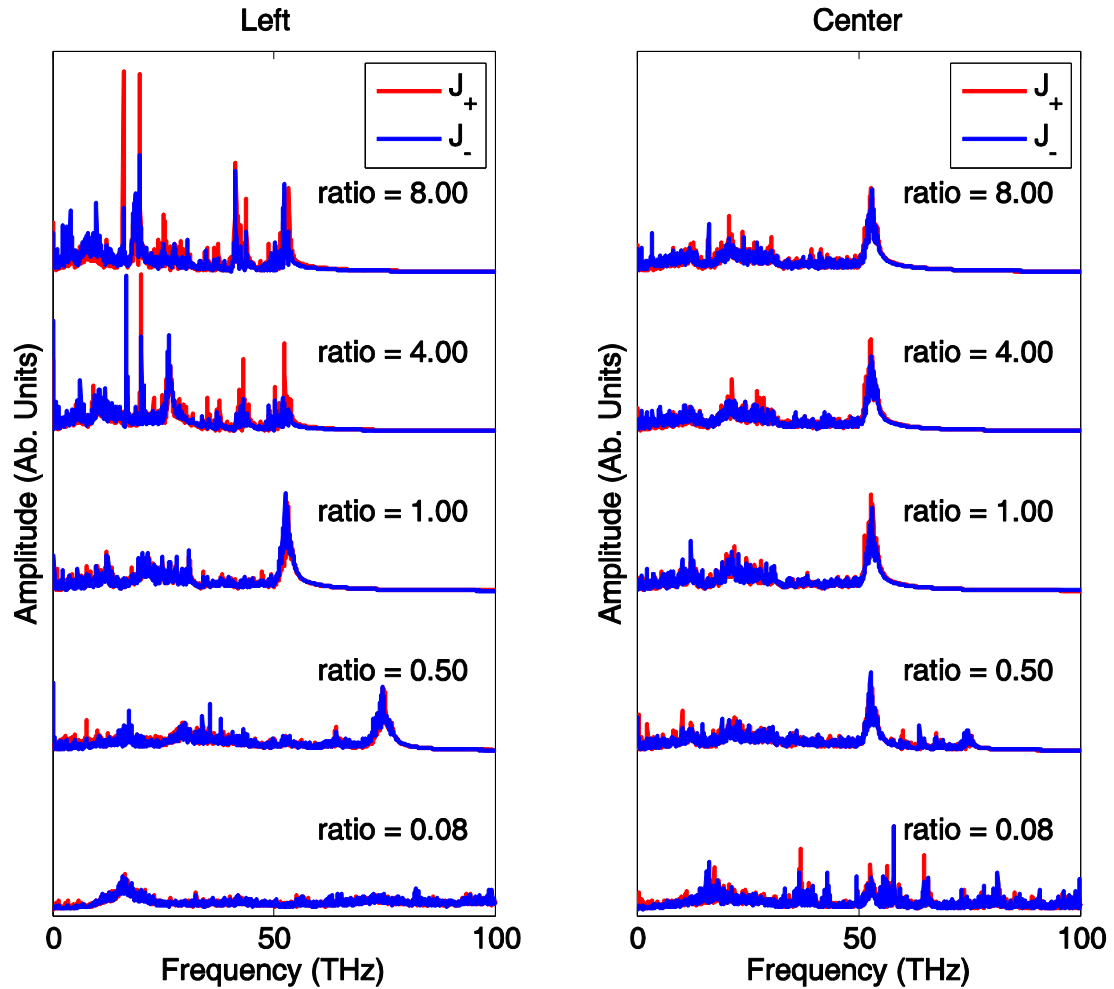


Figure 29 Local PDOS of graphene with various mass ratios in two opposite heat flux directions. Atomic mass ration changes from 0.08 to 8.

with more high frequency phonons on the Left Side to a narrow frequency range in the Center Region. The lower the mass ratio is, the more significant the transmission is. Low frequency phonons have high transmissivity across interface than high frequency phonons [120] and phonons can always transmit from a narrow phonon frequency range into a wide phonon frequency range [121]. Therefore, phonons transmit more easily in J_+ direction when ratio < 1 . Same conclusions can be reached when atomic mass ratio > 1 .

6.3.4 Bonding Strength Effect

The result in Figure 28 shows that the mass gradient is effective in determining thermal rectification of carbon oriented system. However, this mass manipulation is based on ignoring the bond length and bonding strength variation between the dopant and matrix atoms when the mass of dopant varies. On the other hand, based on the lattice dynamics theory, we think the bonding strength of the matrix and matrix-dopant interface plays an important role in the thermal conductivity and thermal rectification. Therefore, we extend

this mass gradient effect study to a different material system with weak bonding strength. To be specific, we adopted AIREBO potential in the previous study for the carbon based 2-D honeycomb structure (graphene). In this section, we will adopt the Tersoff potential to investigate thermal conductivity and thermal rectification

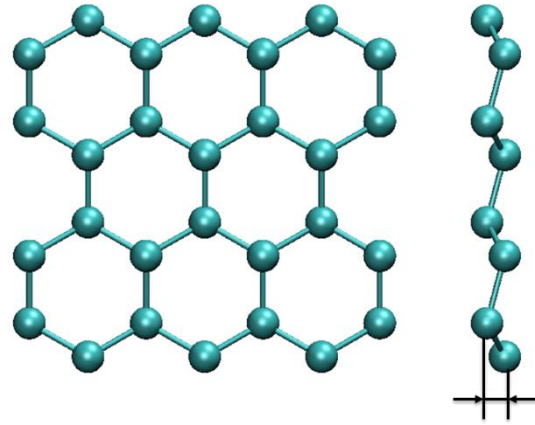


Figure 30 Silicene model with buckled honeycomb lattice structure where Si-Si bond length is 2.28 Å [125], and the buckling parameter δ is 0.45 Å [126]

variation of silicon based 2-D honeycomb structure (silicene [122] [123]). As shown in Figure 30, silicene structure is a buckled 2-D honeycomb structure, which includes two layer of silicon atoms along $\langle 111 \rangle$ direction of bulk silicon.

Table 1 listed the elastic constants of bulk diamond, SiC and silicon, which reflect that the order of bond strength: C-C > Si-C > Si-Si. We adopt Tersoff potential to describe interaction

Table 1 Elastic properties of Carbon, Silicon bonds in Tersoff potential, with unit in Mbar

Property	C-C	Si-C	Si-Si
c_{11}	10.9	4.2	1.5
c_{12}	1.2	1.2	0.8
c_{44}	6.4	2.6	0.7

among silicon atoms and follow the molecular dynamics simulation in section 6.1 to calculate thermal conductivity with two opposite heat flux directions. The simulation box size is 11.5nm×20.2nm. Since graphene and silicene have different atomic mass, same mass ratio is corresponding to different mass difference and mass gradient. We plot thermal conductivity and thermal rectification vs. mass gradient along J_+ direction with the mass gradient defined as,

$$\nabla M = \frac{M_{tri} - M_{mat}}{y_r - y_c} \quad (6.2)$$

where M_{tri} is the atomic mass in triangle doping pattern, M_{mat} is the atomic mass in matrix area, $M_{mat} = 12$ and 28 for graphene and silicene, respectively, y_r is y coordinate of the right edge and y_c is y coordinate of center. As shown in Figure 31, we observe similar trend of thermal conductivity and thermal rectification in silicene structure using Tersoff potential. The thermal conductivity of silicone is much smaller than the thermal

conductivity of graphene, mainly because that silicene has less excitable phonon frequencies than graphene[124]. Similar as previous results, the highest thermal conductivity is reached with pristine silicene. Doping can introduce the thermal conductivity reduction. Thermal rectification has a positive value when mass gradient < 0 (mass ratio < 1) and negative value when mass gradient > 0 (mass ratio > 1), which is consistent with previous results. However, the magnitude of thermal rectification with same mass gradient is smaller within the Tersoff silicene system than the AIREBO carbon system, which become more significant as mass gradient gets even larger. Therefore, the bonding strength plays an important role in thermal rectification. With the same mass gradient, weak bond strength of the system can result in smaller thermal rectification factors.

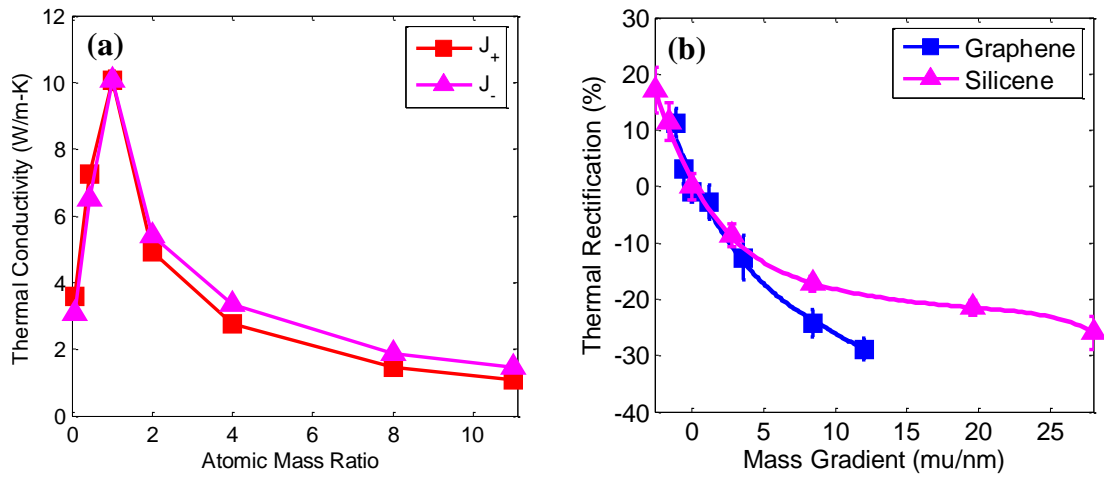


Figure 31 Thermal conductivity (a) of silicene and comparison thermal rectification (b) of silicene and graphene model with triangle doping pattern of various atomic mass

6.3.5 Case Study

In the previous two sections, we study mass effect and bond strength effect on thermal rectification by artificially changing the atomic mass in triangle pattern. Heat conduction prefers mass decreasing direction in both graphene and silicene. From the local PDOS we know that this preference is corresponding to low frequency phonons transmitting to wider frequency range that covers higher frequency phonons. Here we adopt $d\omega$ to represents frequency variation. Base on previous results we can predict the relation between thermal rectification and frequency as,

$$TR \propto d\omega \quad (6.3)$$

With a simple one-dimension monatomic chain model, we can estimate the relation between phonon frequency, mass and force constant by solving the equation of motion as,

$$\omega = \sqrt{\frac{4K}{M}} \left| \sin \frac{ka}{2} \right| \quad (6.4)$$

where ω is frequency, K is force constant, M is the atomic mass, and k is the wave vector. As for a specific wave vector we find,

$$\omega \propto \sqrt{\frac{K}{M}} \quad (6.5)$$

Therefore, we can estimate the relation of TR with M and K as

$$TR = -c_1 dM + c_2 dK \quad (6.6)$$

where c_1 and c_2 are positive coefficients. That means that thermal rectification originates from asymmetry of mass and bond strength (force constant) meanwhile thermal

conductivity in J_+ direction is larger (TR is positive) if this is also the direction of decreasing mass and increasing bond strength.

In order to validate the relation presented in Eq. (6.6), we investigate a real case of silicene matrix with carbon doping model. Tersoff potential is available to describe atomic interaction of C-C, C-Si and Si-Si, respectively, as shown in Fig. 32. We perform NEMD with heat flux in two opposite directions and calculate

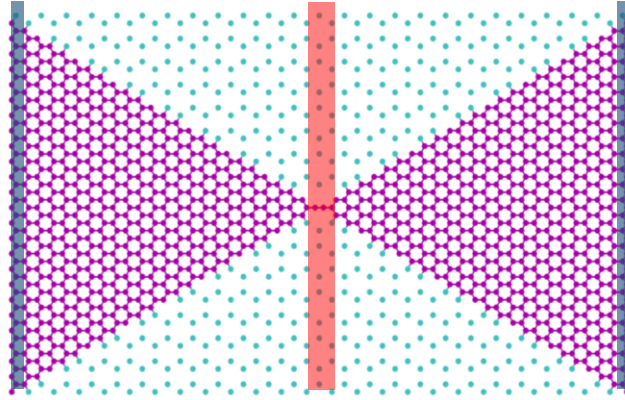


Figure 32 Silicon-Carbon model, carbon atoms are magenta dots in the triangle pattern, silicon atoms the matrix are bonded but not shown in the figure. The red bar and blue bar represent the hot region and cold region, and vice versa.

corresponding thermal conductivity and thermal rectification. In this case, the mass ratio is 0.43. We found that thermal rectification is 23%, which is higher than 11% in pure silicon with mass ratio = 0.43. According to Table 1, the ranking of force constants of different bond styles is $\text{Si-Si} < \text{Si-C} < \text{C-C}$. Thus dK is positive along J_+ direction and increase magnitude of positive TR . The result shows that dK in Eq. (6.6) contributes the extra 12% in thermal rectification comparing to pure silicene where $dK = 0$.

6.4 Summary

In this chapter, we study thermal rectification in graphene with triangle doping pattern and candidate parameters to manipulate thermal rectification factors. The thermal rectification is obtained by comparing thermal conductivity of the same material in two opposite heat flux directions. Thermal rectification is originated from asymmetry of the system in heat flux direction include asymmetry of geometry, strain, size, bonding strength, and atomic mass. Our results show that ensile strain in triangle hydrogen patterned graphene can reduce the effect of doping pattern on thermal rectification. Heat conduction prefers the direction where mass decreases. Higher rectification occurs when atomic mass ratio deviates further from 1 with strong bonding strength. Local phonon density of states in mass gradient system reveals that the difference in PDOS changes with atomic mass ratio. In this work, we investigate an important phenomena in thermal transport in nano-material and identify the parameters that can tune the thermal rectification, which creates a great opportunity to design thermal related nano devices.

CHAPTER 7 CONCLUSIONS

In this thesis, from the perspective of kinetic theory in lattice thermal transport, we investigated thermal transport properties of pristine and doped graphene by using non-equilibrium molecular dynamics method. We studied thermal conductivity of pristine graphene subject to size, strain, chirality and temperature variations. We investigated deformation mode caused by single-side hydrogenation using NEMD simulation and first principle theory. We studied thermal transport properties of double-side doped graphene with different coverage and stripe orientations. By using the SED method, we calculated phonon dispersion, phonon relaxation time and specific heat to analyze doping effect on thermal properties. Finally, we studied thermal rectification of graphene with triangular doping pattern. The conclusions of this work are summarized as follows:

1. We have employed NEMD to study the size, strain, chirality and temperature effects on the thermal transport in pristine graphene. Our results show a significant size dependence of the TC. Thermal conductivity of pristine graphene reduced in higher temperature due to enhanced Umklapp phonon-phonon scattering, which becomes more significant in longer graphene. TC decreases with increasing tensile strain in both zigzag and armchair graphene. Phonon density of states in graphene under tensile strain indicate a red-shift of G-peak, resulting in lower phonon group velocity and a reduction of TC. Our results demonstrate the possibilities of tuning and controlling thermal properties in graphene-based devices by introducing size, strain, chirality and temperature effects.

2. We have demonstrated that a set of different deformation modes of graphene can be formed by the local stresses induced by single-side hydrogenation. Relation between the bending slope of graphene sheet and the length of doping region is explained by the atomic forces calculated from the first principles theory. Thermal conductivity decreases quickly in TRI mode when the W/H ratio increases while it shows an increasing trend under the COM mode. This study shows the possibility to tune thermal conductivity and deformation mode of graphene by using single-side hydrogenation.
3. For double-side hydrogenation, we have studied thermal conductivity variation due to doping stripe coverage and orientation. The TC of hydrogenated graphene has different decreasing trends with different doping stripe orientations. By using the SED method, we calculated phonon dispersion curves which indicate a reduction in phonon group velocity due to hydrogenation. By fitting the Lorentzian function to the phonon SED profile, we evaluated phonon relaxation time and revealed the distinct effect of doping stripe orientations. In addition, it is found that the specific heat has limited contribution to TC reduction caused by hydrogenation.
4. We found that thermal rectification in 2-dimensional nano-material can be tailored by asymmetrical doping pattern, size, strain, atomic mass ratio and bonding strength. Thermal transport prefers in the direction of decreasing mass and

increasing bonding strength. Thermal rectification is higher when mass ratio deviates more from 1 and with weak bonding strength. The local PDOS we employed in mass gradient system shows the difference in area of lighter and heavier atoms and the change with atomic mass ration, which illustrates the cause of rectification from point view of phonon transmission.

REFERENCES

- [1] H. Li and G. Li, “Analysis of ballistic transport in nanoscale devices by using an accelerated finite element contact block reduction approach,” *J. Appl. Phys.*, vol. 116, no. 8, p. 84501, 2014.
- [2] H. Li and G. Li, “Component mode synthesis approaches for quantum mechanical electrostatic analysis of nanoscale devices,” *J. Comput. Electron.*, vol. 10, no. 3, pp. 300–313, 2011.
- [3] C. Lee, X. Wei, J. W. Kysar, and J. Hone, “Measurement of the elastic properties and intrinsic strength of monolayer graphene,” *Science*, vol. 321, pp. 385–388, 2008.
- [4] C. Gómez-Navarro, M. Burghard, and K. Kern, “Elastic properties of chemically derived single graphene sheets,” *Nano Lett.*, vol. 8, pp. 2045–2049, 2008.
- [5] K. S. Novoselov, A. K. Geim, S. V Morozov, D. Jiang, M. I. Katsnelson, I. V Grigorieva, S. V Dubonos, and A. A. Firsov, “Two-dimensional gas of massless Dirac fermions in graphene,” *Nature*, vol. 438, pp. 197–200, 2005.
- [6] Y. Zhang, Y.-W. Tan, H. L. Stormer, and P. Kim, “Experimental observation of the quantum Hall effect and Berry’s phase in graphene,” *Nature*, vol. 438, pp. 201–204, 2005.
- [7] R. R. Nair, P. Blake, A. N. Grigorenko, K. S. Novoselov, T. J. Booth, T. Stauber, N. M. R. Peres, and A. K. Geim, “Fine structure constant defines visual transparency of graphene,” *Science*, vol. 320, p. 1308, 2008.
- [8] A. A. Balandin, S. Ghosh, W. Bao, I. Calizo, D. Teweldebrhan, F. Miao, and C. N. Lau, “Superior thermal conductivity of single-layer graphene,” *Nano Lett.*, vol. 8, no. 3, pp. 902–7, Mar. 2008.
- [9] J. Y. Kim, J.-H. Lee, and J. C. Grossman, “Thermal transport in functionalized graphene,” *ACS Nano*, vol. 6, pp. 9050–7, 2012.
- [10] H. Zhao, K. Min, and N. R. Aluru, “Size and chirality dependent elastic properties of graphene nanoribbons under uniaxial tension,” *Nano Lett.*, vol. 9, no. 8, pp. 3012–3015, 2009.
- [11] H. Zhao and N. R. Aluru, “Temperature and strain-rate dependent fracture strength of graphene,” *J. Appl. Phys.*, vol. 108, no. 6, p. 64321, 2010.

- [12] A. K. Geim, "Graphene: status and prospects.," *Science*, vol. 324, pp. 1530–1534, 2009.
- [13] X. Wang, L. Zhi, and K. Müllen, "Transparent, conductive graphene electrodes for dye-sensitized solar cells," *Nano Lett.*, vol. 8, no. 1, pp. 323–327, 2008.
- [14] K. S. Kim, Y. Zhao, H. Jang, S. Y. Lee, J. M. Kim, K. S. Kim, J.-H. Ahn, P. Kim, J.-Y. Choi, and B. H. Hong, "Large-scale pattern growth of graphene films for stretchable transparent electrodes.," *Nature*, vol. 457, pp. 706–710, 2009.
- [15] "H. Wang, A. Hsu, K.K. Kim, J. Kong, and T. Palacios, in Tech. Dig. - Int. Electron Devices Meet. IEDM (2010)."
- [16] J. Kang, H. Kim, K. S. Kim, S.-K. Lee, S. Bae, J.-H. Ahn, Y.-J. Kim, J.-B. Choi, and B. H. Hong, "High-performance graphene-based transparent flexible heaters.," *Nano Lett.*, vol. 11, no. 12, pp. 5154–8, Dec. 2011.
- [17] J. J. Bae, S. C. Lim, G. H. Han, Y. W. Jo, D. L. Doung, E. S. Kim, S. J. Chae, T. Q. Huy, N. Van Luan, and Y. H. Lee, "Heat Dissipation of Transparent Graphene Defoggers," *Adv. Funct. Mater.*, vol. 22, no. 22, pp. 4819–4826, Nov. 2012.
- [18] A. Yu, P. Ramesh, M. E. Itkis, E. Bekyarova, and R. C. Haddon, "Graphite nanoplatelet-epoxy composite thermal interface materials," *J. Phys. Chem. C*, vol. 111, no. 21, pp. 7565–7569, 2007.
- [19] F. Schedin, A. K. Geim, S. V Morozov, E. W. Hill, P. Blake, M. I. Katsnelson, and K. S. Novoselov, "Detection of individual gas molecules adsorbed on graphene.," *Nat. Mater.*, vol. 6, no. 9, pp. 652–655, 2007.
- [20] K. S. Novoselov, A. K. Geim, S. V Morozov, D. Jiang, Y. Zhang, S. V Dubonos, I. V Grigorieva, and A. A. Firsov, "Electric field effect in atomically thin carbon films.," *Science*, vol. 306, pp. 666–669, 2004.
- [21] "http://www.eurekalert.org/pub_releases/2012-01/uota-nfo010612.php."
- [22] N. Wei, L. Xu, H.-Q. Wang, and J.-C. Zheng, "Strain engineering of thermal conductivity in graphene sheets and nanoribbons: a demonstration of magic flexibility.," *Nanotechnology*, vol. 22, no. 10, p. 105705, Mar. 2011.
- [23] A. Cao, "Molecular dynamics simulation study on heat transport in monolayer graphene sheet with various geometries," *J. Appl. Phys.*, vol. 111, no. 8, p. 083528, 2012.

- [24] T. Y. Ng, J. J. Yeo, and Z. S. Liu, "A molecular dynamics study of the thermal conductivity of graphene nanoribbons containing dispersed Stone–Thrower–Wales defects," *Carbon*, vol. 50. pp. 4887–4893, 2012.
- [25] W. Huang, Q.-X. Pei, Z. Liu, and Y.-W. Zhang, "Thermal conductivity of fluorinated graphene: A non-equilibrium molecular dynamics study," *Chem. Phys. Lett.*, vol. 552, pp. 97–101, Nov. 2012.
- [26] Q. X. Pei, Y. W. Zhang, and V. B. Shenoy, "A molecular dynamics study of the mechanical properties of hydrogen functionalized graphene," *Carbon*, vol. 48. pp. 898–904, 2010.
- [27] B. Mortazavi, A. Rajabpour, S. Ahzi, Y. Rémond, and S. Mehdi Vaez Allaei, "Nitrogen doping and curvature effects on thermal conductivity of graphene: A non-equilibrium molecular dynamics study," *Solid State Commun.*, vol. 152, no. 4, pp. 261–264, Feb. 2012.
- [28] D. W. Boukhvalov and M. I. Katsnelson, "Chemical functionalization of graphene.," *J. Phys. Condens. Matter*, vol. 21, no. 34, p. 344205, Aug. 2009.
- [29] D. C. Elias, R. R. Nair, T. M. G. Mohiuddin, S. V Morozov, P. Blake, M. P. Halsall, A. C. Ferrari, D. W. Boukhvalov, M. I. Katsnelson, A. K. Geim, and K. S. Novoselov, "Control of graphene's properties by reversible hydrogenation: evidence for graphane.," *Science*, vol. 323, pp. 610–613, 2009.
- [30] J. O. Sofo, A. S. Chaudhari, and G. D. Barber, "Graphane: A two-dimensional hydrocarbon," *Phys. Rev. B - Condens. Matter Mater. Phys.*, vol. 75, no. 15, p. 153401, 2007.
- [31] L. a. Chernozatonskii, P. B. Sorokin, E. E. Belova, J. Bruning, and a. S. Fedorov, "Superlattices Consisting of 'Lines' of Adsorbed Hydrogen Atom Pairs on Graphene," vol. 85, no. 1, p. 5, 2007.
- [32] O. V. Yazyev and L. Helm, "Defect-induced magnetism in graphene," *Phys. Rev. B - Condens. Matter Mater. Phys.*, vol. 75, no. 12, p. 125408, 2007.
- [33] H. J. Xiang, E. J. Kan, S. H. Wei, X. G. Gong, and M. H. Whangbo, "Thermodynamically stable single-side hydrogenated graphene," *Phys. Rev. B - Condens. Matter Mater. Phys.*, vol. 82, no. 16, p. 165425, 2010.
- [34] Z. Sun, C. L. Pint, D. C. Marcano, C. Zhang, J. Yao, G. Ruan, Z. Yan, Y. Zhu, R. H. Hauge, and J. M. Tour, "Towards hybrid superlattices in graphene," *Nature Communications*, vol. 2. p. 559, 2011.

- [35] R. Balog, B. Jørgensen, L. Nilsson, M. Andersen, E. Rienks, M. Bianchi, M. Fanetti, E. Laegsgaard, A. Baraldi, S. Lizzit, Z. Sljivancanin, F. Besenbacher, B. Hammer, T. G. Pedersen, P. Hofmann, and L. Hornekaer, “Bandgap opening in graphene induced by patterned hydrogen adsorption.,” *Nat. Mater.*, vol. 9, no. 4, pp. 315–9, Apr. 2010.
- [36] Q.-X. Pei, Z.-D. Sha, and Y.-W. Zhang, “A theoretical analysis of the thermal conductivity of hydrogenated graphene,” *Carbon N. Y.*, vol. 49, no. 14, pp. 4752–4759, Nov. 2011.
- [37] S.-K. Chien, Y.-T. Yang, and C.-K. Chen, “Influence of hydrogen functionalization on thermal conductivity of graphene: Nonequilibrium molecular dynamics simulations,” *Appl. Phys. Lett.*, vol. 98, p. 033107, 2011.
- [38] C. Li, G. Li, and H. Zhao, “Hydrogenation induced deformation mode and thermal conductivity variations in graphene sheets,” *Carbon N. Y.*, vol. 72, no. Md, pp. 185–191, Jun. 2014.
- [39] A. Rajabpour, S. M. Vaez Allaei, and F. Kowsary, “Interface thermal resistance and thermal rectification in hybrid graphene-graphane nanoribbons: A nonequilibrium molecular dynamics study,” *Appl. Phys. Lett.*, vol. 99, no. 5, p. 051917, 2011.
- [40] C. Starr, “The Copper Oxide Rectifier,” *Physics (College. Park. Md.)*, vol. 7, no. 1, p. 15, 1936.
- [41] M. Alaghemandi, E. Algaer, M. C. Böhm, and F. Müller-Plathe, “The thermal conductivity and thermal rectification of carbon nanotubes studied using reverse non-equilibrium molecular dynamics simulations.,” *Nanotechnology*, vol. 20, no. 11, p. 115704, Mar. 2009.
- [42] K. Gordiz and S. Mehdi Vaez Allaei, “Thermal rectification in pristine-hydrogenated carbon nanotube junction: A molecular dynamics study,” *J. Appl. Phys.*, vol. 115, no. 16, p. 163512, Apr. 2014.
- [43] J. Hu, X. Ruan, and Y. P. Chen, “Thermal conductivity and thermal rectification in graphene nanoribbons: A molecular dynamics study,” *Nano Lett.*, 2009.
- [44] J. W. Jiang, J. S. Wang, and B. Li, “Topology-induced thermal rectification in carbon nanodevice,” *EPL (Europhysics Lett.)*, vol. 89, no. 4, p. 46005, Feb. 2010.
- [45] Q. Liang and Y. Wei, “Molecular dynamics study on the thermal conductivity and thermal rectification in graphene with geometric variations of doped boron,” *Phys. B Condens. Matter*, vol. 437, pp. 36–40, Mar. 2014.

- [46] X. Ni, G. Zhang, and B. Li, "Thermal conductivity and thermal rectification in unzipped carbon nanotubes.," *J. Phys. Condens. Matter*, vol. 23, no. 21, p. 215301, Jun. 2011.
- [47] Q.-X. Pei, Y.-W. Zhang, Z.-D. Sha, and V. B. Shenoy, "Carbon isotope doping induced interfacial thermal resistance and thermal rectification in graphene," *Appl. Phys. Lett.*, vol. 100, no. 10, p. 101901, 2012.
- [48] G. Wu and B. Li, "Thermal rectifiers from deformed carbon nanohorns," *J. Phys. Condens. Matter*, vol. 20, no. 17, p. 175211, Apr. 2008.
- [49] G. Wu and B. Li, "Thermal rectification in carbon nanotube intramolecular junctions: Molecular dynamics calculations," *Phys. Rev. B*, vol. 76, no. 8, p. 085424, Aug. 2007.
- [50] N. Yang, N. Li, L. Wang, and B. Li, "Thermal rectification and negative differential thermal resistance in lattices with mass gradient," *Phys. Rev. B*, vol. 76, no. 2, p. 020301, Jul. 2007.
- [51] N. Yang, G. Zhang, and B. Li, "Carbon nanocone: A promising thermal rectifier," *Appl. Phys. Lett.*, vol. 93, no. 24, p. 243111, 2008.
- [52] P. Yang, X. Li, H. Yang, X. Wang, Y. Tang, and X. Yuan, "Numerical investigation on thermal conductivity and thermal rectification in graphene through nitrogen-doping engineering," *Appl. Phys. A*, vol. 112, no. 3, pp. 759–765, Feb. 2013.
- [53] W.-R. Zhong, W.-H. Huang, X.-R. Deng, and B.-Q. Ai, "Thermal rectification in thickness-asymmetric graphene nanoribbons," *Appl. Phys. Lett.*, vol. 99, no. 19, p. 193104, 2011.
- [54] C. W. Chang, D. Okawa, A. Majumdar, and A. Zettl, "Solid-state thermal rectifier," *Science (80-.)*, vol. 314, no. 5802, pp. 1121–1124, 2006.
- [55] R. Yang and G. Chen, "Thermal conductivity modeling of periodic two-dimensional nanocomposites," *Phys. Rev. B - Condens. Matter Mater. Phys.*, vol. 69, no. 19, p. 195316, 2004.
- [56] G. Chen, "Size and Interface Effects on Thermal Conductivity of Superlattices and Periodic Thin-Film Structures," *Journal of Heat Transfer*, vol. 119, no. 2, p. 220, 1997.
- [57] B. H. Armstrong, "883 1981," vol. 23, no. 2, 1981.

- [58] S. V. J. Narumanchi, J. Y. Murthy, and C. H. Amon, "Comparison of Different Phonon Transport Models for Predicting Heat Conduction in Silicon-on-Insulator Transistors," *J. Heat Transfer*, vol. 127, no. 7, p. 713, 2005.
- [59] D. A. Broido, A. Ward, and N. Mingo, "Lattice thermal conductivity of silicon from empirical interatomic potentials," *Phys. Rev. B*, vol. 72, no. 1, p. 14308, 2005.
- [60] G. Chen, "Ballistic-diffusive heat-conduction equations," *Phys. Rev. Lett.*, vol. 86, no. 11, p. 2297, 2001.
- [61] J. Li, L. Porter, and S. Yip, "Atomistic modeling of finite-temperature properties of crystalline β -SiC: II. Thermal conductivity and effects of point defects," *J. Nucl. Mater.*, vol. 255, no. 2, pp. 139–152, 1998.
- [62] W. Zhang, T. S. Fisher, and N. Mingo, "Simulation of Interfacial Phonon Transport in Si--Ge Heterostructures Using an Atomistic Green's Function Method," *J. Heat Transfer*, vol. 129, no. 4, pp. 483–491, 2007.
- [63] D. A. Broido, M. Malorny, G. Birner, N. Mingo, and D. A. Stewart, "Intrinsic lattice thermal conductivity of semiconductors from first principles," *Appl. Phys. Lett.*, vol. 91, no. 23, p. 231922, 2007.
- [64] S. Stuart, A. Tutein, and J. Harrison, "A reactive potential for hydrocarbons with intermolecular interactions," *J. Chem. Phys.*, vol. 112, pp. 6472–6486, 2000.
- [65] D. W. Brenner, O. A. Shenderova, J. A. Harrison, S. J. Stuart, B. Ni, and S. B. Sinnott, "A second-generation reactive empirical bond order (REBO) potential energy expression for hydrocarbons," *J. Phys. Condens. Matter*, vol. 14, no. 4, pp. 783–802, Feb. 2002.
- [66] J. Tersoff, "Modeling solid-state chemistry: Interatomic potentials for multicomponent systems," *Phys. Rev. B*, vol. 39, no. 8, p. 5566, 1989.
- [67] P. Steneteg, *Development of molecular dynamics methodology for simulations of hard materials*, no. 1454. 2012.
- [68] L. Verlet, "Computer 'experiments' on classical fluids. I. Thermodynamical properties of Lennard-Jones molecules," *Phys. Rev.*, vol. 159, no. 1, p. 98, 1967.
- [69] W. G. Hoover, *Computational statistical mechanics*. Elsevier, 2012.
- [70] P. K. Schelling, S. R. Phillpot, and P. Keblinski, "Comparison of atomic-level simulation methods for computing thermal conductivity," *Phys. Rev. B*, vol. 65, no. 14, p. 144306, Apr. 2002.

- [71] D. L. Nika, E. P. Pokatilov, A. S. Askerov, and A. A. Balandin, "Phonon thermal conduction in graphene: Role of Umklapp and edge roughness scattering," *Phys. Rev. B - Condens. Matter Mater. Phys.*, vol. 79, no. 15, 2009.
- [72] D. Şopu, J. Kotakoski, and K. Albe, "Finite-size effects in the phonon density of states of nanostructured germanium: A comparative study of nanoparticles, nanocrystals, nanoglasses, and bulk phases," *Phys. Rev. B - Condens. Matter Mater. Phys.*, vol. 83, no. 24, p. 245416, Jun. 2011.
- [73] A. S. Henry and G. Chen, "Spectral phonon transport properties of silicon based on molecular dynamics simulations and lattice dynamics," *J. Comput. Theor. Nanosci.*, vol. 5, pp. 141–152, 2008.
- [74] L. J. Porter, J. Li, and S. Yip, "Atomistic modeling of finite-temperature properties of β -SiC. I. Lattice vibrations, heat capacity, and thermal expansion," *Journal of Nuclear Materials*, vol. 246, pp. 53–59, 1997.
- [75] H. Bao, B. Qiu, Y. Zhang, and X. Ruan, "A first-principles molecular dynamics approach for predicting optical phonon lifetimes and far-infrared reflectance of polar materials," *J. Quant. Spectrosc. Radiat. Transf.*, vol. 113, no. 13, pp. 1683–1688, Sep. 2012.
- [76] J. E. Turney, J. A. Thomas, A. J. H. McGaughey, and C. H. Amon, "Predicting phonon properties from molecular dynamics simulations using the spectral energy density," in *ASME/JSME 2011 8th Thermal Engineering Joint Conference*, 2011, pp. T30018–T30018.
- [77] D. C. Wallace, "Thermodynamics of Crystals,(1972)." Wiley, Newyork.
- [78] A. J. C. Ladd, B. Moran, and W. G. Hoover, "Lattice thermal conductivity:A comparison of molecular dynamics and anharmonic lattice dynamics," *Phys. Rev. B*, vol. 34, no. 8, pp. 26–44, 1974.
- [79] T. Jadidi, M. Anvari, A. Mashaghi, M. Sahimi, and M. Reza Rahimi Tabar, "Vibrational lifetimes of hydrated phospholipids," *EPL (Europhysics Lett.)*, vol. 102, no. 2, p. 28008, Apr. 2013.
- [80] J. E. Turney, J. A. Thomas, A. J. H. McGaughey, and C. H. Amon, "AJTEC2011-44315 PREDICTING PHONON PROPERTIES FROM MOLECULAR DYNAMICS," *Proc. ASME/JSME 2011 8th Therm. Eng. Jt. Conf.*, 2011.
- [81] W. Rudin, "Real and complex analysis," *Stat.*, vol. 36, no. 4, p. 423, 1987.
- [82] S. Ghosh, I. Calizo, D. Teweldebrhan, E. P. Pokatilov, D. L. Nika, a. a. Balandin, W. Bao, F. Miao, and C. N. Lau, "Extremely high thermal conductivity of graphene:

- Prospects for thermal management applications in nanoelectronic circuits,” *Appl. Phys. Lett.*, vol. 92, no. 15, p. 151911, 2008.
- [83] B. Qiu, H. Bao, G. Zhang, Y. Wu, and X. Ruan, “Molecular dynamics simulations of lattice thermal conductivity and spectral phonon mean free path of PbTe: Bulk and nanostructures,” *Comput. Mater. Sci.*, vol. 53, no. 1, pp. 278–285, Feb. 2012.
 - [84] D. Wei, Y. Song, and F. Wang, “A simple molecular mechanics potential for μm scale graphene simulations from the adaptive force matching method,” *J. Chem. Phys.*, vol. 134, no. 18, p. 184704, May 2011.
 - [85] N. Wei, L. Xu, H.-Q. Wang, and J.-C. Zheng, “Strain engineering of thermal conductivity in graphene sheets and nanoribbons: a demonstration of magic flexibility,” *Nanotechnology*, vol. 22, p. 105705, 2011.
 - [86] Z. Guo, D. Zhang, and X.-G. Gong, “Thermal conductivity of graphene nanoribbons,” *Appl. Phys. Lett.*, vol. 95, no. 16, p. 163103, 2009.
 - [87] B. Mortazavi and S. Ahzi, “Thermal conductivity and tensile response of defective graphene: A molecular dynamics study,” *Carbon N. Y.*, vol. 63, pp. 460–470, 2013.
 - [88] J. Hu, S. Schiffli, A. Vallabhaneni, X. Ruan, and Y. P. Chen, “Tuning the thermal conductivity of graphene nanoribbons by edge passivation and isotope engineering: A molecular dynamics study,” *Appl. Phys. Lett.*, vol. 97, no. 13, p. 133107, 2010.
 - [89] H. Peelaers, A. D. Hernández-Nieves, O. Leenaerts, B. Partoens, and F. M. Peeters, “Vibrational properties of graphene fluoride and graphane,” *Appl. Phys. Lett.*, vol. 98, no. 5, p. 051914, 2011.
 - [90] S. Plimpton, “Fast Parallel Algorithms for Short-Range Molecular Dynamics,” *J. Comput. Phys.*, vol. 117, no. 1, pp. 1–19, 1995.
 - [91] L. Lindsay and D. A. Broido, “Optimized Tersoff and Brenner empirical potential parameters for lattice dynamics and phonon thermal transport in carbon nanotubes and graphene,” *Phys. Rev. B - Condens. Matter Mater. Phys.*, vol. 81, no. 20, p. 205441, 2010.
 - [92] D. W. Brenner, O. A. Shenderova, J. A. Harrison, S. J. Stuart, B. Ni, and S. B. Sinnott, “A second-generation reactive empirical bond order (REBO) potential energy expression for hydrocarbons,” *Journal of Physics: Condensed Matter*, vol. 14, no. 4, pp. 783–802, 2002.
 - [93] G. Kresse, “Efficient iterative schemes for ab initio total-energy calculations using a plane-wave basis set,” *Physical Review B*, vol. 54, no. 16, pp. 11169–11186, 1996.

- [94] G. Kresse and J. Furthmüller, “Efficiency of ab-initio total energy calculations for metals and semiconductors using a plane-wave basis set,” *Comput. Mater. Sci.*, vol. 6, no. 1, pp. 15–50, 1996.
- [95] J. Perdew, K. Burke, and M. Ernzerhof, “Generalized Gradient Approximation Made Simple,” *Phys. Rev. Lett.*, vol. 77, no. 18, pp. 3865–3868, 1996.
- [96] V. N. Popov and P. Lambin, “Radius and chirality dependence of the radial breathing mode and the G -band phonon modes of single-walled carbon nanotubes,” *Phys. Rev. B - Condens. Matter Mater. Phys.*, vol. 73, no. 8, p. 085407, 2006.
- [97] E. Cadelano, P. L. Palla, S. Giordano, and L. Colombo, “Elastic properties of hydrogenated graphene,” *Phys. Rev. B*, vol. 82, no. 23, p. 235414, Dec. 2010.
- [98] M. G. Xia and S. L. Zhang, “Modulation of specific heat in graphene by uniaxial strain,” *Eur. Phys. J. B*, vol. 84, no. 3, pp. 385–390, 2011.
- [99] J. E. Turney, a. J. H. McGaughey, and C. H. Amon, “Assessing the applicability of quantum corrections to classical thermal conductivity predictions,” *Phys. Rev. B - Condens. Matter Mater. Phys.*, vol. 79, no. 22, pp. 1–7, 2009.
- [100] Y. Gao, Y. Jing, Q. Meng, L. Zhang, J. Liu, and X. Qin, “Investigation of the thermal-transport properties for silicon nanofilm covered with graphene via nonequilibrium molecular dynamics,” *Phys. Status Solidi*, vol. 249, no. 9, pp. 1728–1734, Sep. 2012.
- [101] J.-W. Jiang, J. Lan, J.-S. Wang, and B. Li, “Isotopic effects on the thermal conductivity of graphene nanoribbons: localization mechanism,” vol. 054314, no. May 2015, pp. 2–7, 2010.
- [102] L. A. Falkovsky, “Unusual field and temperature dependence of the Hall effect in graphene,” *Phys. Rev. B*, vol. 75, no. 3, p. 33409, 2007.
- [103] F. Liu, P. Ming, and J. Li, “Ab initio calculation of ideal strength and phonon instability of graphene under tension,” *Phys. Rev. B*, vol. 76, no. 6, p. 64120, 2007.
- [104] V. K. Tewary and B. Yang, “Singular behavior of the Debye-Waller factor of graphene,” *Phys. Rev. B*, vol. 79, no. 12, p. 125416, 2009.
- [105] “MRS Bull. 37, 1273 (2012) Pop/Varshney/Roy,” vol. 1273, 2012.
- [106] N. Yang, G. Zhang, and B. Li, “Thermal rectification in asymmetric graphene ribbons,” *Appl. Phys. Lett.*, vol. 95, no. 3, p. 033107, 2009.

- [107] B. Mortazavi, A. Rajabpour, S. Ahzi, Y. Rmond, and S. Mehdi Vaez Allaei, "Nitrogen doping and curvature effects on thermal conductivity of graphene: A non-equilibrium molecular dynamics study," *Solid State Commun.*, vol. 152, pp. 261–264, 2012.
- [108] F. Müller-Plathe, "A simple nonequilibrium molecular dynamics method for calculating the thermal conductivity," *J. Chem. Phys.*, vol. 106, p. 6082, 1997.
- [109] J. Shiomi and S. Maruyama, "Molecular dynamics of diffusive-ballistic heat conduction in single-walled carbon nanotubes," *Jpn. J. Appl. Phys.*, vol. 47, pp. 2005–2009, 2008.
- [110] J. a. Thomas, J. E. Turney, R. M. Iutzi, C. H. Amon, and A. J. H. McGaughey, "Predicting phonon dispersion relations and lifetimes from the spectral energy density," *Phys. Rev. B*, vol. 81, no. 8, p. 081411, Feb. 2010.
- [111] J. M. Larkin and A. J. H. McGaughey, "Predicting alloy vibrational mode properties using lattice dynamics calculations, molecular dynamics simulations, and the virtual crystal approximation," *J. Appl. Phys.*, vol. 114, no. 2, p. 023507, 2013.
- [112] T. Hori, T. Shiga, and J. Shiomi, "Phonon transport analysis of silicon germanium alloys using molecular dynamics simulations," *J. Appl. Phys.*, vol. 113, no. 20, p. 203514, 2013.
- [113] B. Qiu and X. Ruan, "Reduction of spectral phonon relaxation times from suspended to supported graphene," *Appl. Phys. Lett.*, vol. 100, no. 19, p. 193101, 2012.
- [114] M. Wojdyr, "Fityk: a general-purpose peak fitting program," *J. Appl. Crystallogr.*, vol. 43, no. 5, pp. 1126–1128, 2010.
- [115] E. Pop, V. Varshney, and A. K. Roy, "Thermal properties of graphene: Fundamentals and applications," *MRS Bull.*, vol. 37, pp. 1273–1281, 2012.
- [116] N. Mounet and N. Marzari, "First-principles determination of the structural, vibrational and thermodynamic properties of diamond, graphite, and derivatives," *Phys. Rev. B - Condens. Matter Mater. Phys.*, vol. 71, p. 205214, 2005.
- [117] S. Prstic, M. Iyengar, M. Arik, V. Gektin, M. Hodes, S. Narasimhan, and K. Geisler, "Top thermal management innovations from the past 100 years and the next 100 years," *Panel Sess. ITherm2010*, 2010.

- [118] N. Roberts and D. Walker, “Monte Carlo study of thermal transport of direction and frequency dependent boundaries in high Kn systems,” in *Proceedings of ITherm*, 2008.
- [119] J. Hu, X. Ruan, and Y. P. Chen, “Molecular Dynamics Study of Thermal Rectification in Graphene Nanoribbons,” *Int. J. Thermophys.*, vol. 33, no. 6, pp. 986–991, Jun. 2012.
- [120] J. Zhang, Y. Hong, and Y. Yue, “Thermal transport across graphene and single layer hexagonal boron nitride,” *J. Appl. Phys.*, vol. 117, no. 13, p. 134307, 2015.
- [121] B. Liu, J. a. Baimova, C. D. Reddy, S. V. Dmitriev, W. K. Law, X. Q. Feng, and K. Zhou, “Interface thermal conductance and rectification in hybrid graphene/silicene monolayer,” *Carbon N. Y.*, vol. 79, pp. 236–244, 2014.
- [122] B. Lalmi, H. Oughaddou, H. Enriquez, A. Kara, S. Vizzini, B. Ealet, and B. Aufray, “Epitaxial growth of a silicene sheet,” *Appl. Phys. Lett.*, vol. 97, no. 22, p. 223109, 2010.
- [123] B. Aufray, A. Kara, S. Vizzini, H. Oughaddou, C. Leandri, B. Ealet, and G. Le Lay, “Graphene-like silicon nanoribbons on Ag (110): A possible formation of silicene,” *Appl. Phys. Lett.*, vol. 96, no. 18, p. 183102, 2010.
- [124] T. Y. Ng, J. Yeo, and Z. Liu, “Molecular dynamics simulation of the thermal conductivity of shorts strips of graphene and silicene: a comparative study,” *Int. J. Mech. Mater. Des.*, vol. 9, no. 2, pp. 105–114, 2013.
- [125] P. Zhang, X. D. Li, C. H. Hu, S. Q. Wu, and Z. Z. Zhu, “First-principles studies of the hydrogenation effects in silicene sheets,” *Phys. Lett. A*, vol. 376, no. 14, pp. 1230–1233, 2012.
- [126] H. Zhao, “Strain and chirality effects on the mechanical and electronic properties of silicene and silicane under uniaxial tension,” *Phys. Lett. Sect. A Gen. At. Solid State Phys.*, vol. 376, no. 46, pp. 3546–3550, 2012.